

# JGR Solid Earth

## RESEARCH ARTICLE

10.1029/2022JB025936

### Key Points:

- Back-projection and finite fault inversion show the earthquake ruptures bilaterally for ~160 km
- Though the overall rupture speeds on both branches are sub-shear, some patches east of the hypocenter possibly host super-shear ruptures
- The rupture bifurcation at the eastern end can be explained by the regional stress orientation, rupture speed, and fault branching angle

### Supporting Information:

Supporting Information may be found in the online version of this article.

### Correspondence to:

L. Meng,  
lsmeng@g.ucla.edu

### Citation:

Xu, L., Yunjun, Z., Ji, C., Meng, L., Fielding, E. J., Zinke, R., & Bao, H. (2023). Understanding the rupture kinematics and slip model of the 2021 Mw 7.4 Maduo earthquake: A bilateral event on bifurcating faults. *Journal of Geophysical Research: Solid Earth*, 128, e2022JB025936. <https://doi.org/10.1029/2022JB025936>

Received 28 OCT 2022

Accepted 18 MAR 2023

### Author Contributions:

**Conceptualization:** Chen Ji, Lingsen Meng

**Data curation:** Eric J. Fielding

**Formal analysis:** Liuwei Xu, Zhang Yunjun, Chen Ji

**Funding acquisition:** Lingsen Meng, Eric J. Fielding

**Investigation:** Liuwei Xu, Chen Ji

**Methodology:** Liuwei Xu, Zhang Yunjun, Chen Ji, Lingsen Meng, Han Bao

**Project Administration:** Lingsen Meng

**Resources:** Eric J. Fielding, Robert Zinke

**Software:** Liuwei Xu, Zhang Yunjun, Chen Ji, Lingsen Meng, Eric J. Fielding

**Supervision:** Chen Ji, Lingsen Meng

**Visualization:** Liuwei Xu, Zhang Yunjun, Chen Ji

**Writing – original draft:** Liuwei Xu, Zhang Yunjun, Chen Ji, Lingsen Meng

© 2023. American Geophysical Union.  
All Rights Reserved.

## Understanding the Rupture Kinematics and Slip Model of the 2021 Mw 7.4 Maduo Earthquake: A Bilateral Event on Bifurcating Faults

Liuwei Xu<sup>1</sup> , Zhang Yunjun<sup>2</sup> , Chen Ji<sup>3</sup> , Lingsen Meng<sup>1</sup> , Eric J. Fielding<sup>4</sup> , Robert Zinke<sup>4</sup>, and Han Bao<sup>1</sup> 

<sup>1</sup>Department of Earth, Planetary and Space Sciences, University of California Los Angeles, Los Angeles, CA, USA,

<sup>2</sup>Seismological Laboratory, California Institute of Technology, Pasadena, CA, USA, <sup>3</sup>Department of Earth Science, University of California Santa Barbara, Santa Barbara, CA, USA, <sup>4</sup>Jet Propulsion Laboratory, California Institute of Technology, Pasadena, CA, USA

**Abstract** We image the rupture process of the 2021 Mw 7.4 Maduo, Tibet earthquake using slowness-enhanced back-projection (BP) and joint finite fault inversion, which combines teleseismic broadband body waves, long-period (166–333 s) seismic waves, and 3D ground displacements from radar satellites. The results reveal a left-lateral strike-slip rupture, propagating bilaterally on a 160 km long north-dipping sub-vertical fault system that bifurcates near its east end. About 80% of the total seismic moment occurs on the asperities shallower than 10 km, with a peak slip of 5.7 m. To simultaneously match the observed long-period seismic waves and static displacements, potential deep slip is required, despite a tradeoff with the rigidity of the shallow crust. The deep slip existence, local crustal rigidity, and synthetic long-period Earth response for Tibet earthquakes thus deserve further investigation. The WNW branch ruptures ~75 km at ~2.7 km/s, while the ESE branch ruptures ~85 km at ~3 km/s, though super-shear rupture propagation possibly occurs during the ESE propagation from 12 to 20 s. Synthetic BP tests confirm overall sub-shear rupture speeds and reveal a previously undocumented limitation caused by the signal interference between two bilateral branches. The stress analysis on the forks of the fault demonstrates that the pre-compression inclination, rupture speed, and branching angle could explain the branching behavior on the eastern fork.

**Plain Language Summary** A large earthquake struck Maduo county in northeast Tibet on 21 May 2021, with a magnitude of 7.4. To better understand the earthquake rupture and its physics, we use the seismic waveforms from remote stations and surface displacement data from radar satellites to study the rupture geometry, propagation history, and the slip distribution on the fault. Our results show that the earthquake started on the near-vertical Kunlun Pass-Jiangcuo fault and propagated bilaterally both east and west along the fault. The earthquake ruptured a length of ~160 km and moved along the fault at average speeds lower than the shear wave velocity on both sides. The eastern part of the fault included a fork with significant slip on both the north and south branches. This bifurcation behavior can be well explained by the stress direction, rupture speed, and angles between forking faults. Most slip is concentrated at shallow depth, but our estimate for the slip distribution shows that deep slip at the depth of the Tibetan middle crust is required to match all of the observations. The amount of possible deep slip is related to local crust structure and is worthy of more investigation.

## 1. Introduction

The collision of the Indian and Eurasia plates leads to widespread deformation within the Tibet plateau in addition to shortening within the Himalayas. According to earthquake focal mechanisms of  $M > 4$  earthquakes, Yokota et al. (2012) divided the Tibetan plateau into four zones: the northern, eastern, southern, and central zones (Figure 1 inset; Yokota et al., 2012). There are mainly reverse dip-slip earthquakes in the northern and eastern zones, while normal faulting mechanism earthquakes dominate the southern zone. In the central zone, most earthquakes are strike-slip earthquakes. At 18:04, 21 May 2021 (02:04 a.m., 22 May local time), an Mw 7.4 earthquake struck western Maduo county of Qinghai province, a remote area inside the central tectonic zone (Figure 1). The Mw 7.4 Maduo earthquake occurred on the middle portion of the E-W oriented sub-vertical Kunlun Pass-Jiangcuo fault, named in the field investigation after the mainshock. The U.S. Geological Survey

**Writing – review & editing:** Liuwei Xu, Zhang Yunjun, Chen Ji, Lingsen Meng, Eric J. Fielding, Robert Zinke, Han Bao

(USGS) W-phase focal mechanism (USGS, 2022) indicated it was a left-lateral strike-slip earthquake, reminiscent of the two previous super-shear strike-slip earthquakes in Tibet: the 2001 Mw 7.8 Kunlun earthquake and the 2010 Mw 6.9 Yushu earthquake. The 2001 Mw 7.8 Kunlun earthquake ruptured the East-Kunlun fault, a large and active fault in northern Tibet (Wu et al., 2002). The most distinctive property of the Kunlun earthquake was its super-shear rupture speed: between 5 and 6.5 km/s in the center segment (Robinson et al., 2006; Vallée & Dunham, 2012; Wen et al., 2009). The rupture speed of the 2010 Mw 6.9 Yushu earthquake was slightly faster than the shear wave velocity (Yokota et al., 2012; Zhu & Yuan, 2020). This super-shear rupture intensified the ground motion in the forward rupture direction, resulting in severe damage in and around Yushu county (Yokota et al., 2012). The Mw 7.8 Kunlun earthquake and the Mw 6.9 Yushu earthquake occurred on the East Kunlun and Ganzi–Yushu faults, respectively, which were the northern and southern boundary faults of the Bayan Har block. In contrast, the Kunlun Pass-Jiangcuo Fault, where the Mw 7.4 Maduo earthquake occurred, was in the interior of the Bayan Har block.

Several studies have investigated the kinematic rupture history of the Maduo earthquake using back-projection (BP), as well as geodetic and seismic finite fault inversion (FFI) methods (e.g., K. Chen et al., 2022; Jin & Fialko, 2021; Q. Li et al., 2022b; X. Liu et al., 2022b; Lyu et al., 2022; M. Wang et al., 2022b; W. Wang et al., 2022c; Yue et al., 2022; Zhang et al., 2022). The mutually consistent features of these models suggest the earthquake broke a 150–170 km long fault with a peak slip between 4 and 6 m on the fault patch to the east of its epicenter. Though the Maduo earthquake occurred on a left-lateral strike-slip fault and shared a similar focal mechanism to those two super-shear earthquakes mentioned above, its rupture propagated bilaterally, a key difference in comparison with those two unilateral super-shear earthquakes. Previous studies disagreed on whether the Maduo earthquake was a super-shear event. Zhang et al. (2022) found a super-shear rupture speed of 4 km/s on the eastern segment based on BP and far-field Love Mach wave analysis. Yue et al. (2022) proposed that the eastward rupture speed was 4.6 km/s according to the FFI, while another inversion study analyzing high-rate Global Navigation Satellite System (GNSS) data reported a 3.8 km/s eastern rupture (Lyu et al., 2022). On the other hand, the BP study of Q. Li et al. (2022b) suggested that a sub-shear rupture speed was between 1.6 and 3.0 km/s on the western branch, while the rupture speed of the eastern segment was in the range of 2.72–3.67 km/s.

In this study, we construct the 1D velocity model of the source region based on the latest tomography studies (e.g., Han et al., 2021; Xia et al., 2021) and perform the joint FFI using Sentinel-1 Synthetic Aperture Radar (SAR) image displacements and seismic body and surface waveforms to model fault slip evolution on the fault surface. In addition to static displacements in the range direction (e.g., Jin & Fialko, 2021; Zhang et al., 2022), we also include the displacements in the azimuth directions from SAR. We utilize high-frequency *P* wave waveform data from Europe, Australia, and Alaska arrays to perform slowness-enhanced back-projection (SEBP; Meng et al., 2016) analysis, which calibrates the travel time errors using relocated aftershock locations and more accurately constrains the rupture length and speed (Bao et al., 2019). We evaluate the SEBP spatial uncertainty due to incoherent noise via bootstrap tests and validate the overall rupture speeds via synthetic tests. We compare our estimated rupture speeds from SEBP and joint FFI analyses with those reported by studies utilizing multiple-time-windows (MTW) FFI (e.g., Lyu et al., 2022; Yue et al., 2022) and discuss the possibility of super-shear ruptures on some portions of the eastern fault. We analyze the dynamic interactions among multiple fault branches according to the strain rate measurements (M. Wang et al., 2022b), fault geometry, and rupture propagation speeds, which explains the forking behavior during the mainshock. We calculate the Coulomb failure stress (CFS) change (King et al., 1994; Toda et al., 2011) on the left-lateral strike-slip fault surface, compare it with aftershock spatial distribution patterns, and discuss their implications for stress release.

## 2. Finite Fault Inversion

### 2.1. Seismic Waveform Data

We use the joint FFI to image the fault's rupture process and slip distribution (Ji et al., 2003, 2002). We include 30 broadband body-wave recordings (*P* and SH, band-pass filtered between 1 and 200 s), 40 long-period (166–333 s) waveform recordings in vertical and transverse components (dominated by Rayleigh wave and Love wave), and the three-dimensional static surface displacements derived from Sentinel-1 SAR data in the inversion. The seismic data are recorded at teleseismic distances ( $30^\circ < \text{epicenter distance } \Delta < 90^\circ$ ) and obtained from the Incorporated Research Institutions for Seismology (IRIS) data center. The distribution of the selected seismic stations

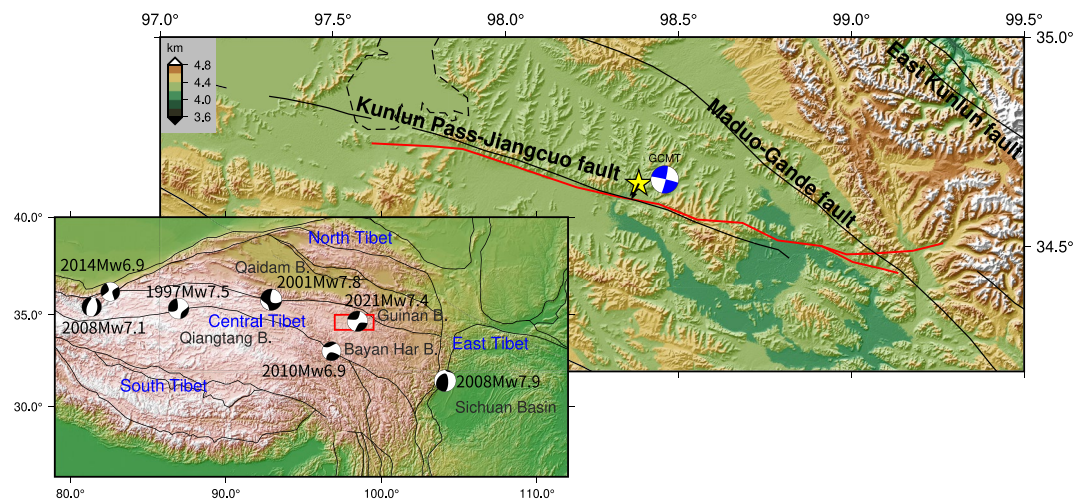


**Figure 1.** Tectonic setting of the 2021 Mw 7.4 Maduo earthquake. The lower left inset shows the major tectonic blocks in the Tibetan plateau and significant historical earthquakes (black beach balls). The red box denotes the study area shown in the main figure. The red line in the main figure shows the rupture trace inferred from the Sentinel-1 range offsets, and the black lines denote the major Tibet faults mapped before this earthquake (Deng, 2007). The yellow star shows the relocated hypocenter ( $34.650^{\circ}\text{N}, 98.384^{\circ}\text{E}$ , depth of 7.6 km; W. Wang et al., 2021). We shift the hypocenter horizontally by 3.9 km following the fault normal direction (black arrow) to  $34.62^{\circ}\text{N}, 98.37^{\circ}\text{E}$  so that this modified hypocenter is on the simplified fault geometry for inversion. The blue beach ball shows the GCMT focal mechanism and centroid location for the 2021 Maduo earthquake.

is shown in Figure S1a in Supporting Information S1, and the selected stations' broadband body and long-period surface waveforms are shown in Figures S1b and S1c in Supporting Information S1, respectively.

## 2.2. SAR Data

We use two pairs of Copernicus Sentinel-1A/B SAR images (from ascending track 99 and descending track 106, both acquired on 20 and 26 May 2021, at 11:26Z and 23:28Z, respectively) to derive the static ground displacement (Figure 2a and Figure S2 in Supporting Information S1). Combining the four displacements from ascending and descending tracks in range (Interferometric SAR, or InSAR) and azimuth (speckle tracking) directions, we construct the 3D ground displacement following Fialko et al. (2001) and Fielding et al. (2020), as implemented in the MintPy software (Yunjun et al., 2019). The SAR acquisition times on 20 and 26 May 2021, tightly bracketed the origin time of the Maduo earthquake (21 May). For the range (cross-track) displacements, we use the ISCE2 software (Fattah et al., 2017; Rosen et al., 2012) for interferogram generation with a Goldstein filter strength of 0.5, the minimum cost flow method of SNAPHU (C. W. Chen & Zebker, 2001) for phase unwrapping guided by a custom mask generated from the spatial coherence with a threshold of 0.4 in the near-fault region (Oliver-Cabrera et al., 2021). We correct the tropospheric delay using the ERA5 weather reanalysis data (Hersbach et al., 2020) via the PyAPS package (Jolivet et al., 2011). For the azimuth (along-track) displacement, we use the GPU-based PyCuAmpcor package within the ISCE2 software for the speckle tracking (also known as amplitude cross-correlation or pixel offset tracking; Michel et al., 1999; Figure S3 in Supporting Information S1). The range offsets are also generated from speckle tracking and used to map the surface rupture traces based on their near-field displacement observations (Figure 2b) but not used in the slip inversion in favor of the redundant and more accurate InSAR observations. The maximum displacements recorded in ascending track 99 (AT099) range offsets, descending track 106 (DT106) range offsets, AT099 azimuth offsets, and DT106 azimuth offsets are 1.36, 1.29, 1.00, and 0.82 m, respectively.

We adopt extra steps to increase the signal-to-noise ratio (SNR) of the SAR azimuth offsets, considering (a) the lower spatial resolution of Sentinel-1 in the azimuth direction than in the range direction (14.1 vs. 2.3 m) and (b) the relatively small displacement in the north-south direction from this dominantly east-west strike-slip faulting. First, we use a large estimation window size of 1,024 by 512 pixels in range and azimuth directions for the cross-correlation to increase its SNR (De Zan, 2014). Second, we correct the SAR processing effects in the azimuth direction (Gisinger et al., 2021) for each subswath by estimating a linear ramp based on the far-field

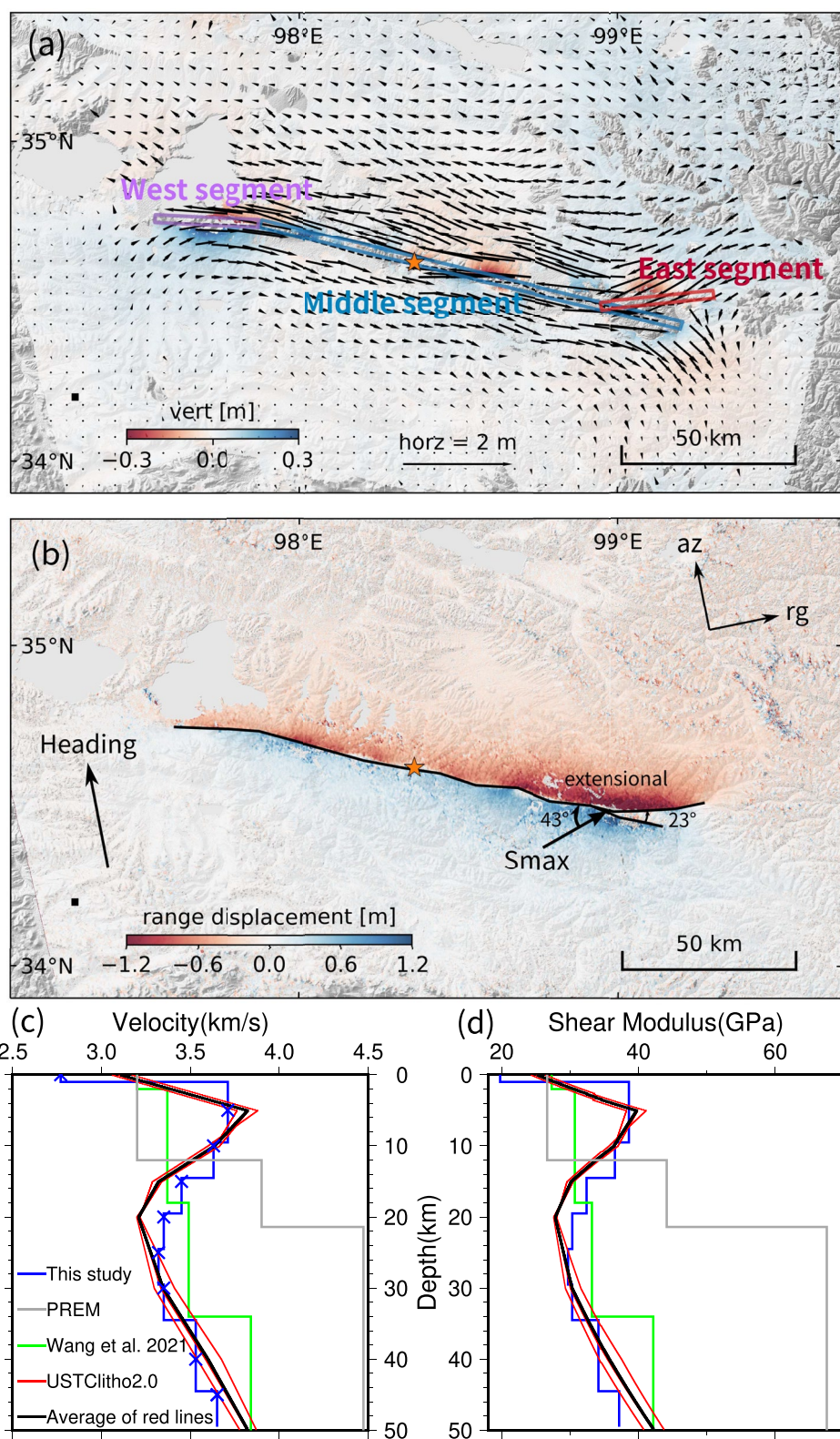


Figure 2.

observation and removing it from the entire subswath. Third, for descending track 106, we apply a median filter with a kernel size of 75 pixels to suppress the high spatial frequency noise (Yun et al., 2007). The improvement of the azimuth displacement is shown in Figure S3 in Supporting Information S1.

These displacement data are further down-sampled with the InSamp software (Lohman & Barnhart, 2010; Lohman & Simons, 2005). We trim the downsampled data points with  $>50$  km distances to the fault surface trace because of their small influence on the inversion. We also remove the points with  $<2$  km distances to the fault trace to avoid the potential location errors of the picked fault traces and simplifications used in the modeled fault segments (Figure S4 in Supporting Information S1).

### 2.3. Modeling, Fault Geometry, and Velocity Structure

To account for the seismic waveform travel-time errors, we first perform a preliminary FFI based on the arrival time of the  $P$  and SH waves predicted using the China Earthquake Administration (CEA) hypocenter (W. Wang et al., 2021) and IASP91 1D velocity model (Kennett & Engdahl, 1991). Then we manually adjust the arrival time so that the predicted waveforms match the observations. We model the fault plane of the Maduo earthquake with three rectangular fault segments: the West, Middle, and East (Figure 2a). The strikes of these fault segments are extracted from our satellite-based surface traces (Figure 2b). We extend these fault planes from the surface to 26 km depth and divide them into 3 km (along the fault) by 2 km (along dip) subfaults. We shift the relocated CEA hypocenter (W. Wang et al., 2021) horizontally by 3.9 km along the fault normal direction to match this simplified fault geometry (Figure 1). We assume these three fault segments share the same fault dip and conduct a series of preliminary inversions to grid search for the optimal dip angle of  $84^\circ$  (Figure 3e). Our simulated annealing FFI method performs the waveform inversion in the wavelet domain and simultaneously inverts for slip amplitude, rupture initiation time, rake angle, and the shape of slip rate function for each subfault (Ji et al., 2002, 2003).

The misfit in low-frequency seismic waves is calculated by combining L1 and L2 norms, while the misfit in high-frequency seismic waves is based on the correlation between predicted and observed waveforms (Sen & Stoffa, 1991). This misfit metric is focused on the signal shape and is well-suited for capturing high-frequency and low-amplitude information. For static displacements, the misfit is calculated by the L2 norm. The range and azimuth displacements are weighted based on the reciprocals of observation uncertainty. The inversion aims to minimize the weighted sum of the seismic and geodetic residuals, with regularization constraints to reduce the difference between the slip on adjacent subfaults and to reduce the total seismic moment (Hartzell et al., 1996). The weighting of the individual data sets and strength of the constraints are obtained on a trial-and-error basis, balancing the tradeoff between the resolution and inversion stability. In our procedure, all inversions begin from random initial fault slip models with total moment equal to the result of the point source inversions (e.g., Global CMT catalog). Inversions with individual data sets and no constraints are first performed to determine the maximum possible improvements, which are then used to normalize the misfit in the future joint inversion (Ji et al., 2002).

Since the rupture speeds measured by SEBP analysis in Section 3 are 3.0 and 2.7 km/s for eastward and westward rupture propagation, we allow the rupture velocity in the inversion to vary between 1.5 and 3.5 km/s. We construct a 1D crustal velocity model in the source region (Figure 2c) by interpolating a regional  $P$  and  $S$  waves tomography model of northeast Tibet (Xia et al., 2021). The crustal density and shear modulus are inferred from seismic velocity based on the empirical relationships from laboratory measurements (Brocher, 2005; Gardner et al., 1974). This crustal model features a high-velocity upper crust and low-velocity mid-crust, consistent with other recent tomography models (e.g., USTClitho2.0, Han et al., 2021; Figure 2c). The synthetic seismograms of body waves are calculated using first motion approximation (Langston & Helmberger, 1975), while the normal mode superposition algorithm is used to compute the synthetic long-period surface wave seismograms (e.g., Dahlen & Tromp, 1999). We implement 800 simulated annealing iterations for each of our inversions. In the final

**Figure 2.** Static ground displacement from Synthetic Aperture Radar (SAR) and velocity and rigidity models. (a) 3D deformation map for the source region (as shown in Figure S2 in Supporting Information S1). The arrows represent the horizontal deformation, and the color shows the vertical deformation. The orange star denotes the epicenter used in this study. The colored rectangular boxes show the surface projections of the preferred fault model's West, Middle, and East segments. (b) Range displacements from SAR speckle tracking in ascending track 99. Black lines represent the surface traces picked based on range displacements.  $S_{\max}$  is the maximum compressive principal stress (W. Wang et al., 2022b). The black square represents the reference point ( $34.2^\circ\text{N}, 97.3^\circ\text{E}$ ). (c) Velocity models as a function of depth. Different colors denote models from different studies. Red lines show the 1D models beneath the selected nodes (Figure S5 in Supporting Information S1) of the USTClitho2.0 model (Han et al., 2021). The black line is the average of red lines. Crosses on the blue line are control points from Xia et al. (2021). (d) Rigidity models.

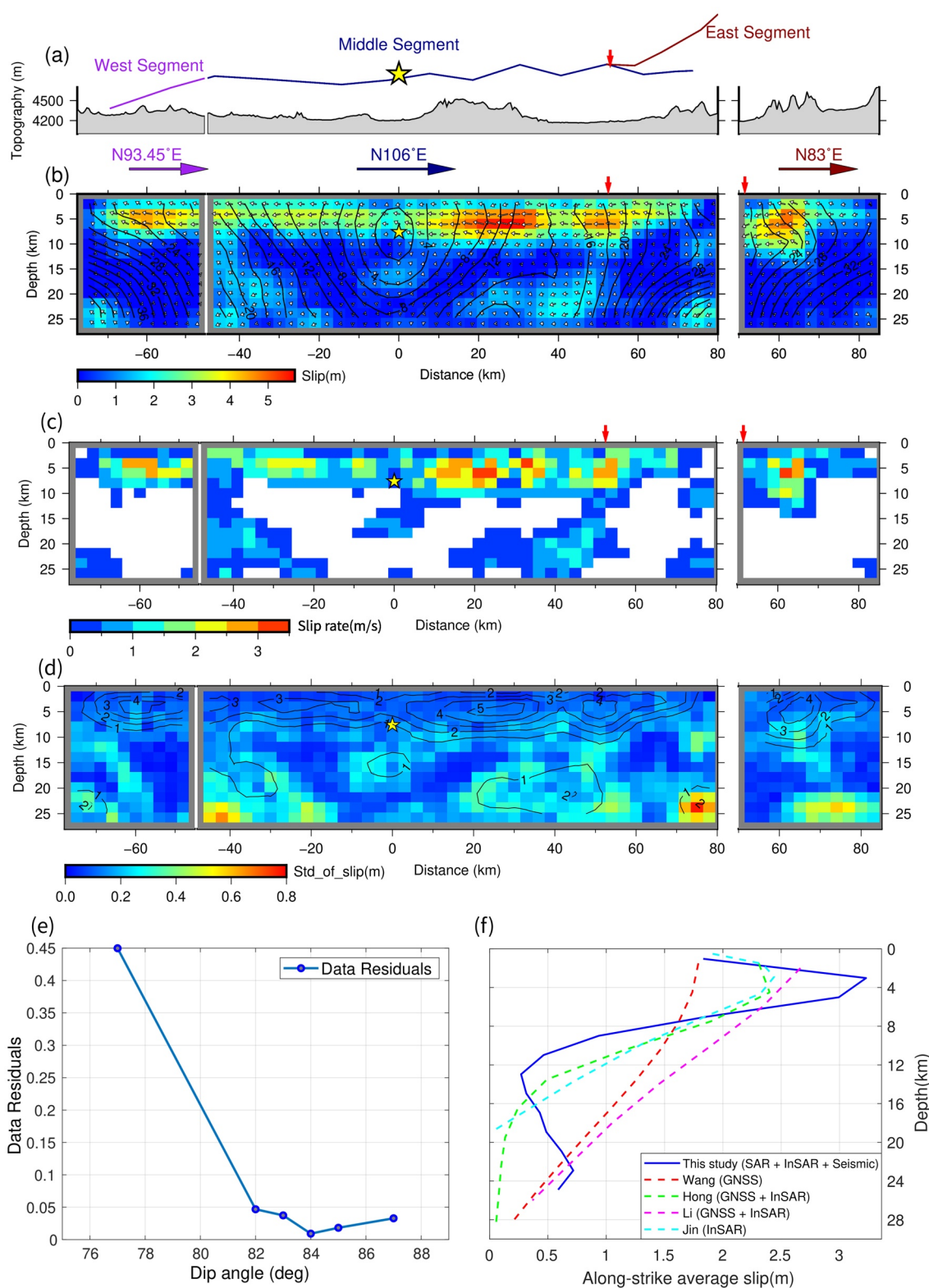


Figure 3.

20 iterations, the objective function values for the selected models oscillate within  $\pm 0.3\%$  of their mean, suggesting the inversion has converged to a stable solution.

#### 2.4. Finite Fault Results

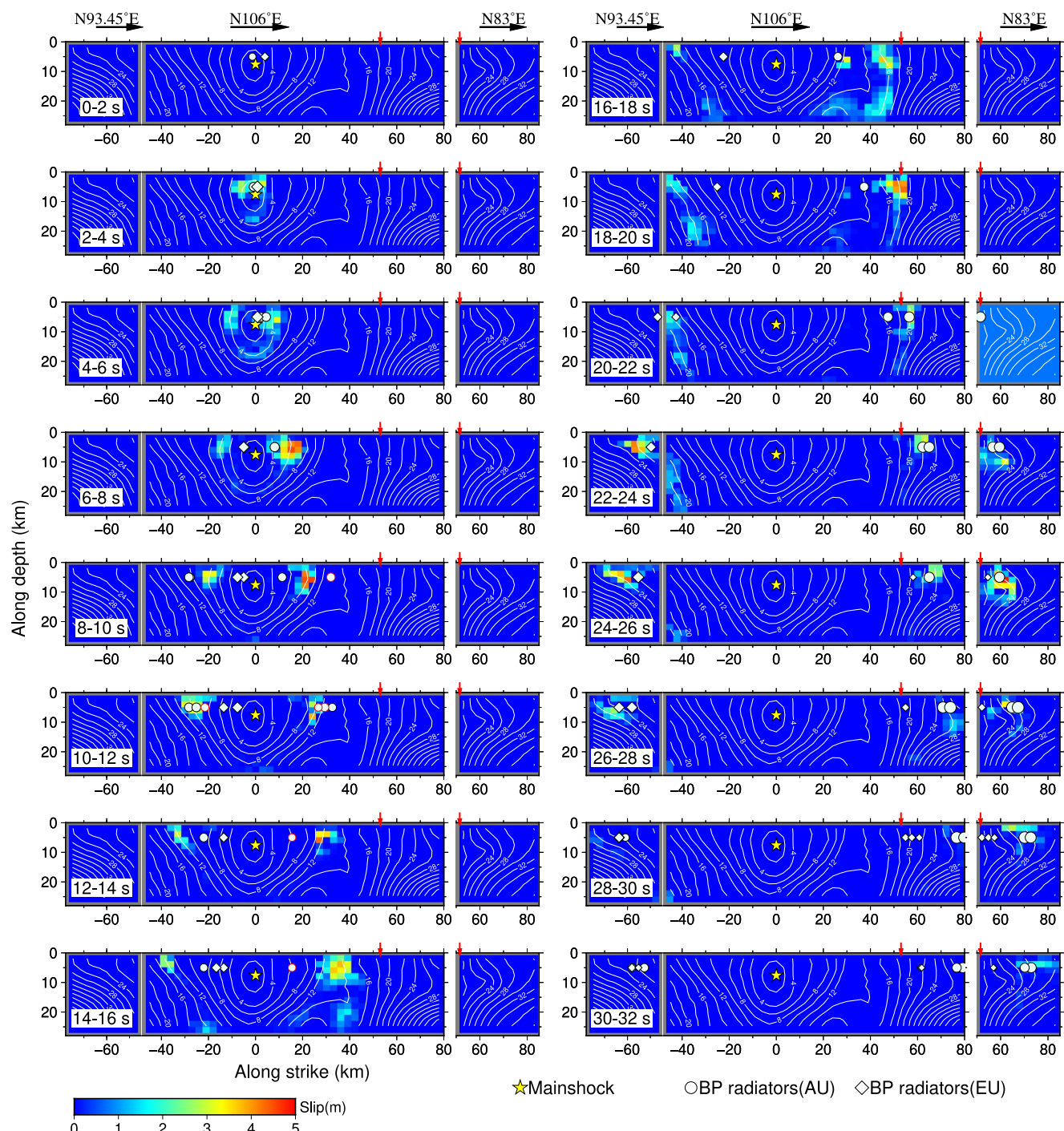
The solutions of simulated annealing inversions often depend slightly on the selected random seed, especially when there are multiple optimal solutions within the model space with indistinguishable objective function values. The different random seeds lead to different initial fault models and Markov chains. We have conducted 10 inversions with different random seeds to explore this uncertainty. As expected, all of them reach similar minimum objective function values. Relative to the average, the standard deviation (STD) of these 10 objective function values is negligible compared with their average value ( $\sim 0.1\%$  of the average). All of the 10 models are then the plausible solutions for this earthquake. The inverted model with the smallest objective function value is chosen to be the preferred model presented below. As summarized in Figure 3, our joint FFI inversion reveals a bilateral rupture. Both seismic and geodetic data favor a slightly north-dipping fault geometry with an optimal dip angle of  $84^\circ$  (Figure 3e). The rupture model features a total seismic moment of  $1.83 \times 10^{20}$  Nm, yielding an Mw estimate of 7.44. Most of the slip occurs in the shallow crust with a depth of  $\le 10$  km, which accounts for 77% of the total seismic moment. There are two large-slip patches on the eastern part of the Middle segment, centered at 20 and 50 km from the hypocenter, with peak slip values of 5.7 and 4.5 m, respectively. The slip on the western part of the Middle segment is shallower and relatively uniform, with an average of  $\sim 3$  m. Significant slip is also seen on the splay faults, with peak slips of 4.2 and 5 m on the West and East segments. Beyond the eastern bifurcation point, the peak slip on the East segment is more significant than that on the Middle segment continuation on the south side of the fork. Figure 3f shows the along-strike average slip variation with depth. Similar to some previous results (e.g., Hong et al., 2022; Jin & Fialko, 2021), our model shows a significant shallow slip deficit in the top 2 km, where the average slip reduces by 43% from 3.2 to 1.8 m.

Figure 4 and Movie S1 show the snapshot of the slip and the rupture process in 2 s intervals. It can be seen that after rupture nucleating at the modified CEA hypocenter mentioned above, the rupture propagates bilaterally on the Middle segment at a speed 2.4–2.5 km/s, migrating 28–30 km on both sides for about 12 s (Figure 4). The rupture front propagates to the east much faster in the next 6 s, then arrives at the intersections of the branching faults at 18 s for both ruptures. In the 20–32 s interval, the western rupture steps onto the West segment, while the eastern rupture simultaneously breaks the East and Middle east-continuation segments. Based on the rupture initiation time contours, we obtained an average rupture velocity of  $\sim 3$  km/s for the eastern propagation and  $\sim 2.7$  km/s for the western propagation, respectively (Figure 4 and Figure S6 in Supporting Information S1). The average slip rate, defined as the final slip amplitude over the rise time at each subfault, is shown in Figure 3c. The larger slip rate correlates with the more significant slip in the first order.

We validate the results by comparing predictions from our preferred model with both seismic (Figure S1 in Supporting Information S1) and geodetic observations (Figures S7 and S8 in Supporting Information S1), both of which show good matches overall. For the geodetic data, misfits are concentrated near the surface traces and the terminal ends, likely due to local undulations of the fault geometry. Misfits for range displacements (from InSAR) are smaller than those for azimuth displacements (from speckle tracking) because the inversion puts larger weights on InSAR due to their smaller observational uncertainty. Our forward prediction of the horizontal displacements also satisfactorily matches the observation of 27 near-fault GNSS stations not used in the inversions (D. Wang et al., 2022a; M. Wang et al., 2022b; Figure S9 in Supporting Information S1).

We explore the uncertainty of the solution by analyzing the results of the FFIs with different random seeds. Figure 3d shows the STD among the 10 inverted slip models for each subfault. The mean and maximum STD is 0.15 and 0.8 m (2.6% and 14% of the maximum slip), respectively. The average slip STD of individual subfaults

**Figure 3.** The preferred slip distribution of the 2021 Maduo earthquake. (a) The fault traces and the topography along the fault traces of the Maduo earthquake. (b) The slip distribution of the preferred model. The horizontal arrows and words on top display the orientations of three fault segments. Red vertical arrows indicate the intersection of the Middle and East segments. White arrows indicate slip vectors. Contours display the rupture initiation time. (c) Average slip rate distribution on the fault. It is defined as the slip amplitude (in meter) divided by the rise time (in second). Only the subfaults with  $>0.57$  m slip (10% of the maximum slip) are displayed. The rise time of a subfault with negligible slip is often poorly constrained (Ji et al., 2002). (d) The standard deviation of the fault slip among the 10 plausible slip models. The contours show their average. (e) Relative data residuals as a function of the assumed fault dip angle. (f) Compilation of the along-strike average coseismic slip as a function of depth (Hong et al., 2022; Jin & Fialko, 2021; Q. Li et al., 2022b; M. Wang et al., 2022b). For simplicity, only the first author's name and the used data type are indicated.



**Figure 4.** Snapshots of the preferred model at 2 s time intervals, which are indicated at the lower left corner of each snapshot. The yellow star shows the hypocenter. White circles and diamonds denote the high-frequency radiators resolved by the slowness-enhanced back-projection analyses using the Australia and Europe arrays, respectively.

increases with depth (Figure 3d). While the slip STDs on individual subfaults are sensitive to the subfault size (e.g., Fialko et al., 2001), the along-strike average slip (the blue line in Figure 3f) is much more stable. The STDs of the along-strike averages are also depth dependent but only up to 0.05 m on the downdip edge of the fault plane (Figure S10 in Supporting Information S1).

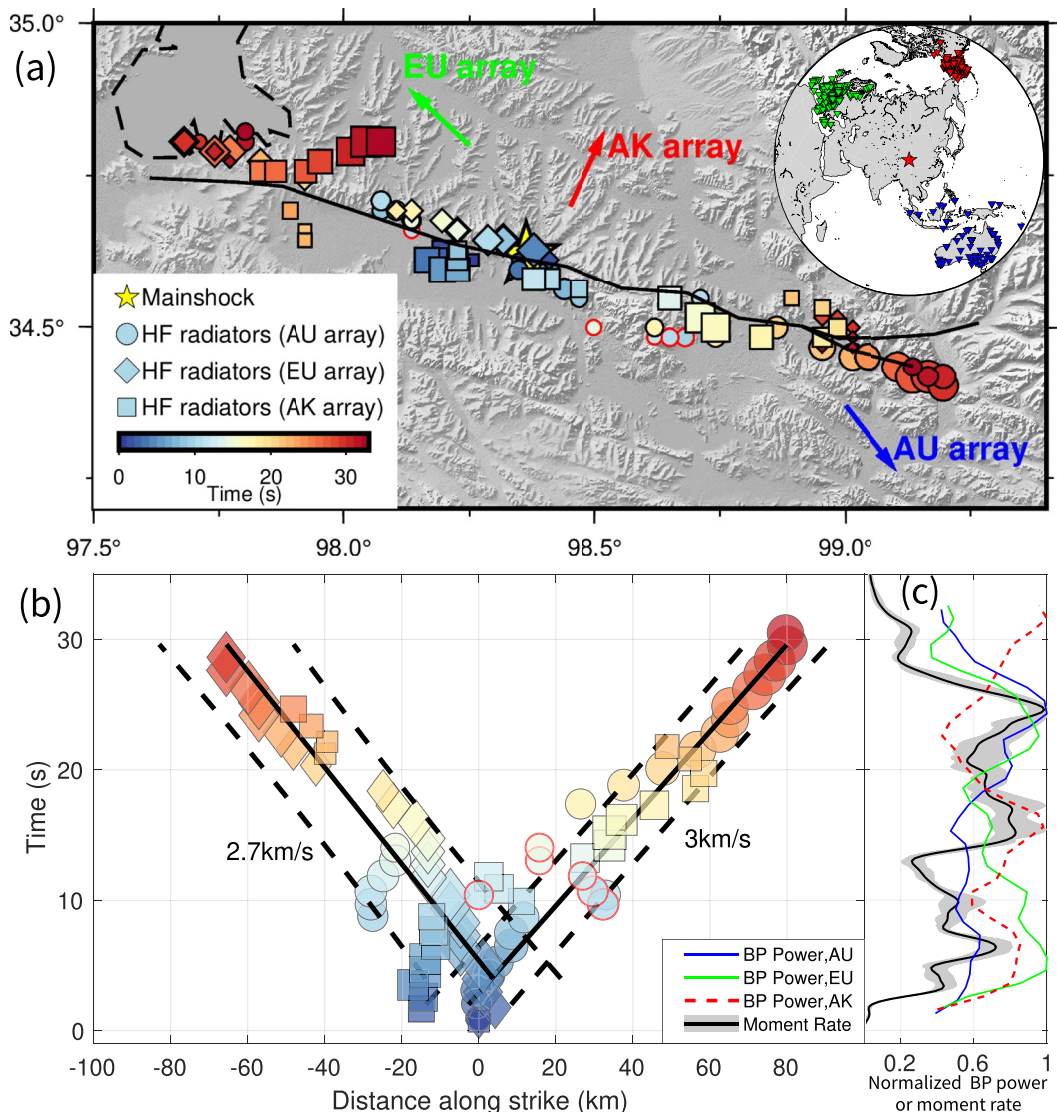


**Figure 5.** Summary of back-projection results. (a) High-frequency (HF) radiators imaged by the three arrays. Circles, diamonds, and squares are HF radiators imaged by the AU, EU, and AK arrays, respectively, and color-coded by rupture time. Circles with red edges are manually picked secondary radiators. Inset on the upper-right: stations used in the slowness-enhanced back-projection analysis. (b) Along-strike ( $N106^{\circ}E$ ) location and timing of the radiators. Black solid and dash lines represent rupture speeds and uncertainties estimated based on linear regressions, respectively. Numbers show the estimated rupture speed. (c) Comparison between back-projection (BP) power and moment rates. Blue, green, and red lines represent the BP power of the AU, EU, and AK arrays. The black line and the gray area represent the average and the range of moment rates of the 10 plausible models.

### 3. Slowness-Enhanced Back-Projection

BP is a popular source-imaging technique that tracks the growth of earthquake ruptures based on coherent seismic wavefields recorded by dense networks (e.g., Kiser & Ishii, 2017). Meng et al. (2012, 2011) improved BP by introducing the Multiple Signal Classification (MUSIC) techniques, which yielded sharper and more robust source images than conventional beamforming approaches. The SEBP further improved MUSIC BP by correcting the travel time error in the entire source region caused by the heterogeneity of the 3D Earth structure (Bao et al., 2019; Meng et al., 2018, 2019, 2016). Because the SEBP utilizes seismic signals in higher frequency contents than FFI, the two methods provide complementary views of an earthquake rupture process.

### 3.1. Data and Processing

The SEBP analysis utilizes seismic data at teleseismic distances ( $30^\circ < \Delta < 90^\circ$ ). We obtained the data from IRIS and Observatories and Research Facilities for European Seismology (ORFEUS). For the Maduo earthquake, three large-aperture arrays are available in the teleseismic distance range: Australia (AU, 90 stations), Alaska (AK, 153 stations), and pan-Europe (EU, 401 stations) (upper-right inset in Figure 5a). We use the vertical component of broadband seismograms and band-pass filter the seismograms between 0.5 and 2 Hz, the highest frequency range with enough waveform coherence and adequate SNR. We adopt a 12 s long sliding window to balance the temporal resolution and robustness. The time step is set to 1 s. Seismograms are normalized by their initial  $P$  arrivals at all stations.

The rupture directivity modulates the apparent rupture time during large earthquakes. The wave train is compressed for the receiver station in the forward direction, and the apparent rupture time becomes earlier than the true rupture time. In contrast, the wave train is stretched in the backward direction, which leads to a later apparent rupture time than the true time. Such an effect leads to a distorted estimation of source durations and rupture speeds. To correct the directivity effect, we first calculate the travel time from a given rupture point to the stations and the travel time from the hypocenter to the stations. We then deduct their mean difference at all stations from the apparent rupture time to obtain the actual rupture time (Du, 2021; Yao et al., 2011).

Standard BP adopts the travel times predicted by the 1D reference Earth model. We obtain the “hypocenter correction” by cross-correlating the initial window of  $P$  phase arrivals, which reduces the travel time errors caused by the 3D path effects of the Earth structure (Ishii et al., 2005). However, for large earthquakes, the hypocenter correction becomes less effective at source regions far from the hypocenter. To mitigate the entire source region’s spatial errors resulting from the path effects, we apply the SEBP that accounts for the travel times’ spatial derivatives along the rupture path (Bao et al., 2019; Meng et al., 2018, 2016).

For the 2021 Mw 7.4 Maduo earthquake, we select three  $M \geq 4.7$  events to ensure sufficient SNR between 0.5 and 2 Hz. These three events distribute over the mainshock rupture path (Figure S11 in Supporting Information S1), and their differential  $P$  wave travel times with respect to the hypocenter are compared with those computed based on the 1-D Earth model. The leftover travel time differences and the distances between the mainshock and aftershocks are then utilized to derive the slowness correction terms. Accurate locations of these events are crucial for reliable slowness calibrations. Thus we adopt a relocated CEA catalog created using a double-difference method (Waldhauser & Ellsworth, 2000) and seismic recordings at 53 stations within 400 km (W. Wang et al., 2021). Figure S11 in Supporting Information S1 shows the comparison between the BP-inferred event locations before and after the slowness calibration: the correction reduces the root-mean-square distances between the BP-inferred location and catalog location from 11.92 to 2.03 km, from 2.84 to 1.74 km and from 7.60 to 3.75 km for AU, EU, AK arrays, respectively.

### 3.2. Back-Projection Results

The spatiotemporal progression of the rupture process imaged by SEBP analysis using the AU, EU, and AK arrays are shown in Figure 5a by circles, diamonds, and rectangles, respectively. The SEBP analysis images energetic BP radiators for approximately 32 s after the rupture initiation (Figure 5c), consistent with the rupture duration resolved by joint FFI. The rupture propagates bilaterally, extending in the ESE-WNW directions. The west branch breaks a ~70 km long segment while the east branch ruptures an ~80 km long branch. Figure 5b plots the along-strike ( $N106^\circ E$ ) rupture locations versus rupture time. The average rupture speeds of the west and east propagations are 2.7 and 3.0 km/s, respectively. Compared with BP radiators before slowness correction (Figure S12 in Supporting Information S1), the SEBP radiators of the three arrays are more mutually consistent and conform to the surface fault trace better, indicating the effectiveness of the slowness correction. Most of the time, the AU array only resolves the east branch (Movie S2), while the EU array images the west branch (Movie S3). The AK array images both branches equally well because of its sub-perpendicular orientation to the fault strike (Movie S4). Such an array-dependent effect is expected for bilateral ruptures: the seismic radiations from the proximal branch have shorter wavelengths due to Doppler effects, leading to stronger apparent high-frequency beam power (B. Li et al., 2022a). Exceptions occur from 9 to 15 s, during which the SEBP analysis using the AU array identifies both primary and secondary peaks that correspond to the separated fronts of bilateral rupture (Movie S2). We manually pick the location and time of the secondary peaks, as shown by the circles with red edges in Figures 5a and 5b.

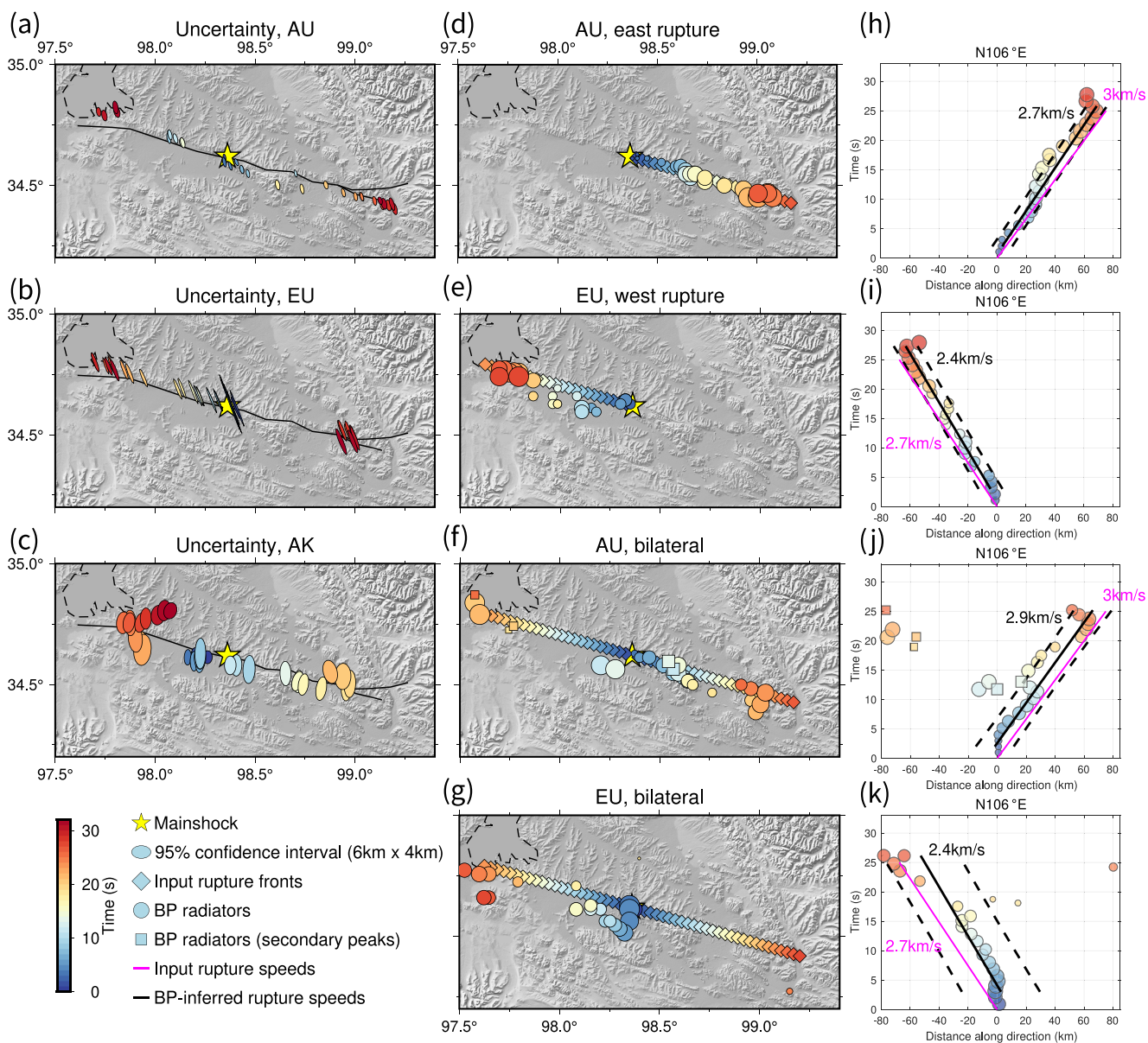


**Figure 6.** Back-projection (BP) uncertainty tests and synthetic tests. (a–c) BP uncertainties for the AU, EU, and AK arrays due to incoherent noise. The colors and shapes of the ellipses demonstrate the BP timing and the 95% confidence interval on the peak locations. The ellipse in the legend demonstrates the reference uncertainty with 6 km on the major axis and 4 km on the minor axis. The yellow stars indicate the epicenter. (d–g) The setup of the synthetic tests and the corresponding BP results. The spatial-temporal evolutions of BPs (circles) are plotted over the input rupture fronts (diamonds). BP radiators are color-coded by time, and the symbol size represents the normalized power. (h–k) Along-strike locations and rupture time of BP radiators. The rupture time is relative to the origin time. Location is the horizontal position relative to the epicenter, projected along the N106°E. Squares are secondary radiators manually picked. Pink lines and numbers indicate the input rupture speeds. Black solid lines and numbers are estimated rupture speeds based on linear regressions, with black dashed lines representing estimation uncertainties of linear regressions.

### 3.3. Uncertainty of Back-Projection Due To Incoherent Noise

To estimate the uncertainty caused by coda waves, local scattering, and heterogeneous site effects, we bootstrap the BP by adding randomized noise to the coherent signals. We estimate the noise amplitude spectrum based on the incoherent part of the waveforms. First, the peak in the SEBP image is defined as a reference point-source location at each time step. At each time window, we obtain the mean seismogram (as a proxy of the coherent arrival) by aligning, stacking, and averaging the array waveforms according to the time shift predicted by the reference location. We compute the waveform residual with respect to the mean seismogram, which is then

regarded as incoherent noise at each station. We randomize the Fourier phase spectrum of the incoherent noise and add it back to the mean seismogram. This procedure is designed to model the random phases of scattering waves while retaining the amplitude spectrum of the waveform. One hundred synthetic realizations of the mean seismogram plus incoherent noise are then back-projected to obtain the perturbed BP locations for each time step. Figures 6a–6c show the ellipses representing the 95% confidence-bound on the BP radiator locations. We find that the major axes of the uncertainty ellipsis generally point toward the receiver array, indicating a more significant uncertainty along the radial direction (toward the array) than the tangential direction. The median length of the major and minor axes are 3.0 by 1.2 km, 6.6 by 0.8 km, and 7.4 by 3.6 km for AU, EU, and AK arrays, respectively. These analyses suggest that the uncertainty of the three arrays is reasonably small. Among them, the AU BP is the most reliable, probably due to its largest array aperture; The EU BP has a small tangential uncertainty but a moderate radial uncertainty; the AK BP has moderate uncertainty in both the radial and tangential directions. We note the uncertainty becomes much larger near 32 s for the EU and AK BPs, which indicates that the coherent waveform is diminishing and incoherent coda starts to dominate the wavefield. Therefore we consider the rupture duration determined by SEBP analysis is 32 s, consistent with the rupture duration derived by FFI.

### 3.4. BP-Inferred Rupture Speeds of Bilateral Ruptures

BP radiators are proxies of rupture fronts (Ishii et al., 2005). Thus tracing their spatial and temporal evolution allows us to estimate rupture speeds. For unilateral ruptures, such a procedure is usually accurate (e.g., Bao et al., 2019; Meng et al., 2016). However, for bilateral ruptures, the interference between the seismic signals emitted from the two rupture fronts might distort the rupture speed estimation, especially at the beginning of the earthquake when the two fronts are closely spaced. To evaluate the impact of this interference, we design and conduct synthetic tests considering both unilateral and bilateral scenarios. The tests include four cases: (a) a unilateral rupture to the east imaged using the AU array (Figure 6d); (b) a unilateral rupture to the west imaged using the EU array (Figure 6e); (c) a bilateral rupture imaged using the AU array (Figure 6f); (d) a bilateral rupture imaged using the EU array (Figure 6g). To mimic the Maduo earthquake, we assume a 26 km wide vertical fault with an 80 km east fault branch and a 70 km west branch relative to the hypocenter. The rupture speeds on the east and the west fault branches are set to 3.0 and 2.7 km/s, respectively. To understand the performances of the BP analysis for heterogeneous ruptures, we discretize the fault plane into 1 km by 1 km subfaults and adopt the slip distribution derived by our joint FFI (Figure 3b). The Yoffe analytic function (Tinti et al., 2005; Yoffe, 1951) with a constant 5 s rise time is used as the slip-rate function. We calculate the synthetic waveforms as the sum of slip-rate contributions from each subfault convolved with empirical Green's functions (EGFs, Table S1 in Supporting Information S1).

As Figures 6d–6k show, in cases 1 and 2, the recovered speeds for the unilateral ruptures are 2.7 and 2.4 km/s, respectively, slightly slower (~10%) than the input rupture speeds. We conclude that for the unilateral rupture, the BP analysis can image the locations of rupture fronts and measure the propagation speeds as expected (Figures 6d, 6e, 6h, and 6i). However, for cases of bilateral rupture (Figures 6f, 6g, 6j, and 6k), most of the time the BP analysis only identifies the rupture propagation on one fault branch, with the AU array for the east branch and the EU arrays for the west branch. This occurs during the early stage of the rupture when the separation of the two fronts is below the resolution limit of the array (the minimum separable distance of two closely spaced sources). The rupture front captured by the BP analysis tends to be the one propagating toward the receiver array since the shorter wavelength due to Doppler effects leads to stronger apparent high-frequency beam power (B. Li et al., 2022a). In the late rupture stage ( $t > 20$  s), the BP analysis can solve the radiators corresponding to both rupture fronts. The overall rupture speeds on the east and the west fault branches imaged by the BP analysis in cases 3 and 4 (bilateral cases) are 2.9 and 2.4 km/s, respectively, which are also slightly slower than the input rupture speeds. The results indicate that the overall speeds are reliable if we include all leading radiators. However, the locations of BP radiators during the early stage seem to be affected by the signal interference of the two rupture fronts and the array resolution limit. We find that the BP analysis using either the AU array or the EU arrays shows apparent rupture stagnation in the first several seconds. There are also artificial rupture jumps between 8 and 18 s in the BP results using the AU array. Therefore, caution needs to be taken when interpreting the rupture speeds of small segments, especially in the early stage of a bilateral rupture. We note that such an issue only occurs in particular bilateral rupture scenarios. For unilateral rupture or the late stage of bilateral ruptures when source separations are large enough, the rupture speed can be reasonably estimated by following the timing and locations of the leading BP radiators.

## 4. Discussion

### 4.1. Possible Deep Slip and Its Tradeoff With Shallow Rigidity

We compare the along-strike average slip from our preferred slip model with that of other published models (Hong et al., 2022; Jin & Fialko, 2021; Q. Li et al., 2022b; M. Wang et al., 2022b; Figure 3f). Those published models were derived using different data sets (SAR, InSAR, GPS, and seismic waves) and crustal models (half-space Earth or CRUST1.0). However, none of them included the constraint from long-period seismic waves. It can be seen that the along-strike average slip in all models reaches a maximum at a depth of 1–4 km, beneath which it decreases with depth (Figure 3f). Most models (e.g., Hong et al., 2022; Jin & Fialko, 2021), including ours, show a significant shallow slip deficit in the top 2 km. However, there are notable differences in the maximum along-strike average slip (1.7–2.7 m in other studies and ~3.2 m in ours) and the depth extent of the coseismic slip (19–28 km; Figure 3f). From a depth of 13–24 km, the along-strike average slip of our preferred model increases to ~0.7 m (~22% of the maximum).

For the convenience of discussion, hereafter we refer to the fault slip on the subfaults shallower than 10 km as the “shallow” slip and the rest as the “possible deep” slip, according to the sensitivity of static observations. We call the deep slip “possible” because the distribution and amplitude of deep slip are less well constrained by the geodetic data, as indicated by the large uncertainties on individual subfaults (Figure 3d). However, the deep slip cumulatively contributes 23% of the total seismic moment. This moment percentage is stable, varying from 22% to 24% among the 10 plausible solutions. Without the deep slip, the synthetic amplitude of long-period (166–333 s) seismic waves is about 23% smaller than the observations (Figure S13 in Supporting Information S1). This is expected because the amplitude of long-period seismic waves is directly proportional to the total seismic moment of the entire rupture (e.g., Kanamori & Given, 1981). Removing the deep slip also has negative impacts to the fits of teleseismic body waves (Figure S14 in Supporting Information S1) and especially geodetic data (Figure S15 in Supporting Information S1). To explore the effect from fault width settings, we follow Aderhold and Abercrombie (2016) and perform inversions with 36, 20, 16, 14, 12, and 10 km wide faults (Figure S16 in Supporting Information S1). As shown in Figures S16 and S17 in Supporting Information S1, when the fault widths are greater than or equal to 14 km, the shallow slip distribution and the shallow average slip patterns are similar for all models. But when the fault width is reduced to 12 km or less, the shallow slip is distorted. In the case of a 10 km wide fault, the along-strike average slip reaches the maximum below 5 km, which is notably deeper than that in other wider models. In the meantime, the average slip at the downdip edge of the fault plane exceeds 1.5 m, indicating that the data requires a wider fault plane. On the other hand, the fits to all data sets become worse when we adopt narrower faults (Figure S18 in Supporting Information S1). For long-period waves, the average ratio between synthetic waveform amplitudes and observed waveform amplitudes reduces from 1.00 to 0.92 as the model width reduces from 26 to 10 km (Figure S19 in Supporting Information S1), roughly equivalent to an 8% deficit in the synthetic seismic moment. Above tests suggest that a relatively wide fault (e.g., 26 km) and some deep slip are necessary to preserve the slip distribution features in the shallow fault and to fit the multiple data sets. Nevertheless, both the geodetic and seismic data could not well constrain the exact depth and distribution of the deep slip.

An alternative explanation is that the deep slip is the artifacts caused by current under-estimation on source region's crust rigidity. For joint FFI inversions using both near-fault geodetic data and long-period seismic data, we identify a tradeoff between the deep slip and the rigidity in the shallow crust by comparing slip solutions using two different 1D velocity models: one from W. Wang et al. (2021), and one modified from Xia et al. (2021). The former has a slower upper crustal shear wave speed (3.4 km/s at depths of 2–18 km) than the latter (our preferred model, 3.7 km/s at depths of 1–10 km; Figure 7e). Their difference in rigidity is more significant, about 18% if averaging over the top 10 km. The results are shown in Figures 7b and 7a. Compared with our preferred model (Figure 7a), the inverted model using the velocity model of W. Wang et al. (2021) (Figure 7b) has essentially the same along-strike average slip in the shallow depth, but the along-strike average slip on the deep subfaults increases by about 30% (Figure 7f). This tradeoff between the deep slip and shallow rigidity can be simply explained by the seismic moment calculation, which is a product of the fault slip, fault patch area, and surrounding rock's rigidity (shear modulus). Unlike long-period seismic data, in the first order, near-fault geodetic data is sensitive to the seismic potency (the product of fault slip and fault area) rather than the seismic moment. Then without affecting the fits to geodetic data, the match to the long-period seismic waves with the shallow fault slip can be improved if we use a velocity model with higher rigidity in the shallow depth. However, to fully compensate for 23% of the total seismic moment,

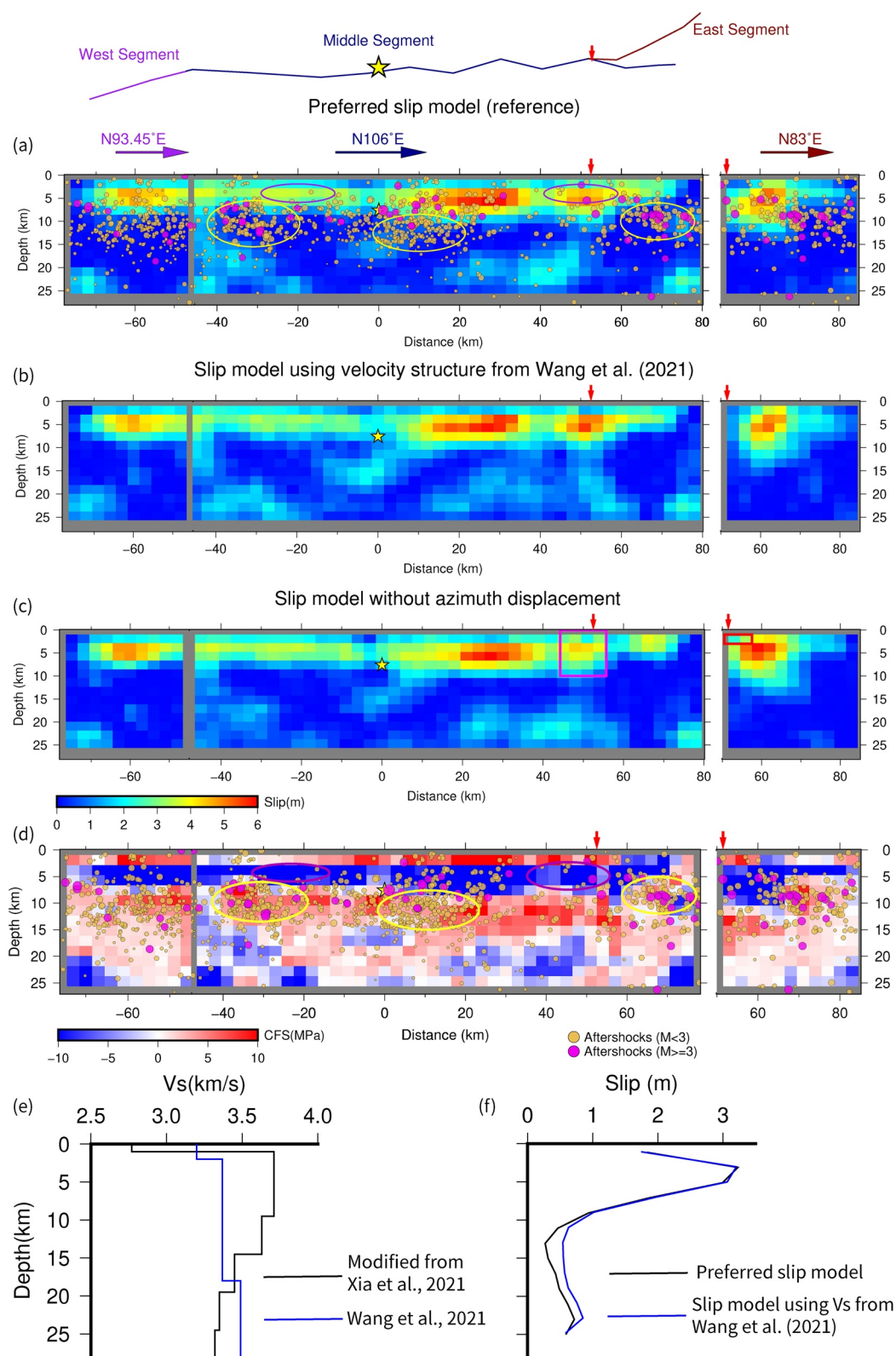


**Figure 7.**

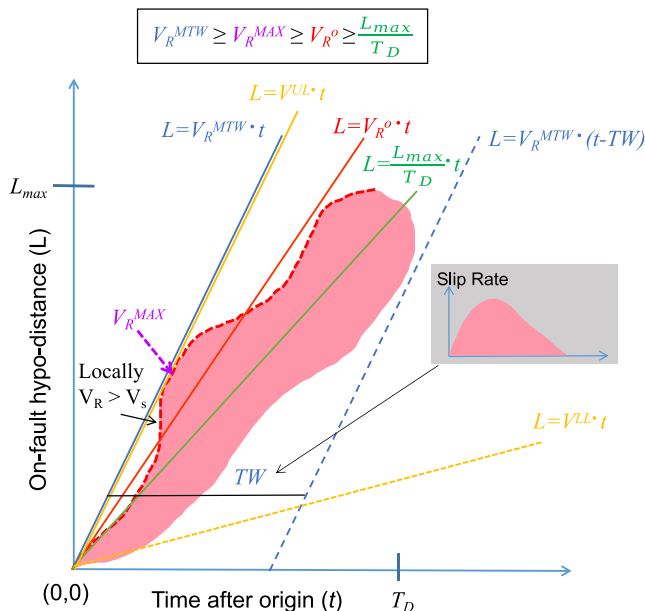


**Figure 8.** Definitions of four types of rupture velocity estimate discussed in the text: multiple time window finite fault inversion  $V_R^{MTW}$ ; the fastest “apparent” rupture velocity relative to the hypocenter during fault rupture  $V_R^{MAX}$ ; overall rupture velocity  $V_R^o$ ; and the ratio of rupture length and rupture duration  $L_{max}/T_D$ ; the upper limit of the rupture velocity in our nonlinear inversion  $V^{UL}$ ; the lower limit of the rupture velocity in our nonlinear inversion  $V^{LL}$ .

dashed line denotes the projection of the rupture front. This line can be curved, reflecting that the “apparent” rupture velocity relative to the hypocenter (i.e.,  $L/t$ ) during the rupture evolution is not constant. One can fit the curved red dashed line with a straight line from the hypocenter (the solid red line in Figure 8). Its slope is the overall rupture velocity ( $V_R^o$ ) we discussed above. During our nonlinear FFI, the time when one point on the fault surface starts to slip is one of the inverted parameters (e.g., Ji et al., 2003, 2002). Its spatial variation is shown as white contours in Figure 4.

Our nonlinear FFI algorithm requires a reference speed, an upper limit speed ( $V^{UL}$ ), and a lower limit speed ( $V^{LL}$ ), which is 3, 3.5, and 1.5 km/s, respectively. In this study,  $V^{UL}$  and  $V^{LL}$  appear as orange solid and dash lines in Figure 8, and the region encompassed by them should contain light-red areas. Our reference speed of 3 km/s is determined according to  $V_R^o$  measured by the SEBP analysis. However, as we model the slip rate function as a single analytic time function, the solution is sensitive only to the majority portion of the fault rupture. On the other hand, finite fault studies of K. Chen et al. (2022), Lyu et al. (2022), Yue et al. (2022), and Zhang et al. (2022) adopted the MTW FFI method originally proposed by Hartzell and Heaton (1983). In the MTW approach, the non-zero slip rate at one point on the fault surface is allowed only within  $(L/V_R^{MTW}, L/V_R^{MTW} + TW)$ , where rupture velocity  $V_R^{MTW}$  and time window  $TW$  are pre-assigned inversion parameters. In other words, the slip is only allowed after a propagating front with a speed of  $V_R^{MTW}$ , therefore by definition, the  $V_R^{MTW}$  is the maximum possible rupture speed allowed in such inversion (Hartzell & Heaton, 1983). In Figure 8, solid and dashed blue lines show this temporal limitation for the fault rupture.  $V_R^{MTW}$  and  $TW$  must be properly selected so that the light red patch falls between these two lines. Readers shall be aware that the value of  $V_R^{MTW}$  for an earthquake reported

the shear wave speed in the shallow depth needs to furtherly increase by over 10%, which may be unrealistic. Another potential contributor may be that the synthetic long-period seismic response calculation using the 1D PREM model (Dziewonski & Anderson, 1981) is systematically lower for earthquakes in the Tibet plateau, which features an abnormally thick crust (e.g., Kind et al., 2002; Z. Liu et al., 2021). Therefore, the existence and magnitude of deep slip deserve further investigation when an accurate crustal velocity and rigidity model in this source region becomes available.

## 4.2. Rupture Velocity Definitions Used in the Literature

Our estimated average rupture speeds from the hypocenter on the west and east fault branches are 2.7 and 3.0 km/s, respectively. The measurements are consistent with the finite fault analysis by K. Chen et al. (2022) and the BP study by Q. Li et al. (2022b), which found that the rupture speed for the east fault was in the range of 2.72–3.67 km/s and was between 1.39 and 3.17 km/s on the western fault. In contrast, several source studies reported a fast rupture propagation to the east, with the rupture speed varying from 3.8 to 4.6 km/s (Lyu et al., 2022; W. Wang et al., 2022c; Yue et al., 2022; Zhang et al., 2022).

Before exploring the cause of these discrepancies, it is important to review the rupture velocity definitions used in these studies. In Figure 8, the horizontal axis denotes the time after the rupture origin ( $t$ ), and the vertical axis shows the on-fault hypocenter distance of a point on the fault surface ( $L$ ). One can project every point on the coseismic fault plane to this diagram and use the light-red color to highlight the period when this point experiences non-zero slip rates (Figure 8 inset). The light-red patch is the projection for the entire rupture (Figure 8). By definition, the

**Figure 7.** Comparison between slip models inverted with different 1D Vs structures and with different displacement data. (a) The preferred slip model inverted with the 1D velocity structure modified from Xia et al. (2021), the same as Figure 3b. Light brown and magenta dots denote the  $M < 3$  and  $M \geq 3$  aftershocks, respectively, with size proportional to the magnitude. Purple and yellow hollow ellipses highlight regions with sparse and dense aftershocks, respectively. (b) Slip model inverted using the 1D velocity structure adopted in W. Wang et al. (2021). (c) Slip model inverted without Synthetic Aperture Radar azimuth displacements. The magenta and red boxes denote the compared regions mentioned in Section 4.4. (d) Coulomb failure stress change on the fault planes. Purple and yellow hollow ellipses highlight regions with negative  $\Delta CFS$  and positive  $\Delta CFS$ , respectively. (e) S wave velocity structure adopted in the preferred model (black line, modified from Xia et al., 2021) and in W. Wang et al. (2021) (blue line). (f) Along-strike average slip as a function of depth. Black and blue lines represent the preferred slip model and the model using the S wave velocity model of W. Wang et al. (2021), respectively.

in the literature is sensitive to TW. When there is no limit on TW, in principle  $V_R^{\text{MTW}}$  can be any value larger than or equal to  $V_R^{\text{MAX}}$ , the fastest “apparent” rupture velocity measured from the hypocenter that is achieved during the earthquake rupture (Figure 8). However, to make the FFI stable, researchers often try to use a TW as small as possible. Only when TW is limited can an optimal  $V_R^{\text{MTW}}$  be found through a grid search (see Figure 2 in Yue et al., 2022). Finally, if one uses  $L_{\max}$  and  $T_D$  to define the total rupture length and the total rupture duration for the eastward rupture during the Maduo earthquake, their ratio  $L_{\max}/T_D$  is also a proxy of rupture velocity. Considering the intrinsic differences among the definitions of  $V_R^{\text{MTW}}$ ,  $V_R^{\circ}$ , and  $L_{\max}/T_D$  (Figure 8), in principle the inequality  $V_R^{\text{MTW}} \geq V_R^{\text{MAX}} \geq V_R^{\circ} \geq L_{\max}/T_D$  shall hold. But when TW is small, the optimal  $V_R^{\text{MTW}}$  reported by an MTW FFI analysis can even be smaller than  $V_R^{\circ}$ .

$L_{\max}/T_D$  is the lower bound of  $V_R^{\circ}$ . For the eastward branch of the rupture propagation during the Maduo earthquake,  $L_{\max}$  ( $\sim 85$  km) is well constrained by geodetic data. Ours (Figure 3b and Figures S6 and S20 in Supporting Information S1) and many other FFIs (K. Chen et al., 2022; Lyu et al., 2022; Zhang et al., 2022) reveal a rupture duration ( $T_D$ ) of about 32 s. The ratio  $L_{\max}/T_D$  is then 2.66 km/s, lower than our estimated speed of 3.0 km/s for the east rupture. It is noteworthy that for such a long fault branch, a  $V_R^{\circ}$  much faster than  $L_{\max}/T_D$  often suggests a long rise time. For example, if  $V_R^{\circ}$  is 4 km/s, the rupture front will reach the east end of the Maduo rupture in  $\sim 21$  s, suggesting either the rise time of the fault rupture is about 11 s or delayed secondary fault ruptures with significant slip. It is of interest to note that for such a long strike-slip rupture, the maximum rise time inferred from the dynamic calculation is  $W/(2V_R^{\circ})$ , where  $W$  is the fault width (Day, 1982).

$V_R^{\text{MTW}}$  can be viewed as the upper bound of  $V_R^{\circ}$ . Besides TW, the published  $V_R^{\text{MTW}}$  estimates of the Maduo earthquake (K. Chen et al., 2022; Lyu et al., 2022; Yue et al., 2022; Table S2 in Supporting Information S1) suggest that the reported  $V_R^{\text{MTW}}$  is sensitive to the hypocenter location, another piece of a priori information used during the FFI source studies. Yue et al. (2022) reported the largest  $V_R^{\text{MTW}}$  (4.6 km/s) for the eastward rupture and the smallest  $V_R^{\text{MTW}}$  (2 km/s) for the westward rupture in the literature. We notice that Yue et al. (2022) adopted the Preliminary Determination of Epicenters location (98.255°E, 34.586°N, 10 km; Table S2 in Supporting Information S1) reported by National Earthquake Information Center, USGS, which is 10–13 km west of the Chinese Earthquake Network location (98.354°E, 34.624°N, 8 km; Table S2 in Supporting Information S1) or relocated CEA location (98.385°E, 34.650°N, 7.6 km, W. Wang et al., 2021) used by other studies. As we discussed above, the majority of fault slip during this earthquake is well constrained by the geodetic data. It is seismic data that constrains the temporal rupture evolution relative to the hypocenter. Then a westward offset of the hypocenter will increase the on-fault hypocenter distances for the asperities on the east side of the hypocenter but decrease the on-fault hypocenter distances for the asperities on the west side. The estimates of rupture velocity are then expected to be higher to the east and lower to the west. Hence, accurate hypocenter location is crucial in retrieving kinematic rupture parameters, such as rupture speed, even when the fault slip is well-constrained.

#### 4.3. Super-Shear Possibility

One outstanding question about the Maduo earthquake is whether the rupture speed is super-shear. In our selected 1D velocity model (Figure 7e), the average shear wave speed (Vs) within the top 10 km is 3.7 km/s. According to our SEBP analysis and FFI results, the average rupture speeds of both ESE and WNW branches are sub-shear, approximately 73% and 81% of the local shear wave speed, respectively. However, some FFI and BP studies found super-shear propagation speeds on the east rupture (Lyu et al., 2022; W. Wang et al., 2022c; Yue et al., 2022; Zhang et al., 2022). Table S2 in Supporting Information S1 summarizes the eastward rupture speeds reported by these studies. Among them, Yue et al. (2022) reported the largest  $V_R^{\text{MTW}}$  of 4.6 km/s, while Zhang et al. (2022) utilized BP to obtain a  $V_R^{\circ}$  of 4 km/s. Lyu et al. (2022) carried out an MTW FFI using geodetic and seismic data. Their seismic data set also included high-rate GNSS data. They found that the best waveform fit to one GNSS record (QHAJ station in Figure S9 in Supporting Information S1) was achieved when  $V_R^{\text{MTW}}$  of the eastward rupture propagation was 3.8 km/s. Because all other data could be well explained with a  $V_R^{\text{MTW}}$  of 2.8 km/s, they claimed that this earthquake features an overall sub-shear but locally super-shear rupture.

Rupture propagation on the fault plane of a natural earthquake is often not in constant velocity (Figure 8). Although our result shows that overall the rupture propagation of the Maduo earthquake is sub-shear, we do not exclude the super-shear possibility on some portions of Middle or East segments. Figures 3b and 4 show that from 12 to 20 s, the eastern rupture front traveled from  $\sim 28$  to  $\sim 58$  km, suggesting a local rupture propagation speed of  $\sim 3.8$  km/s. This is slightly higher than the average shear wave speed of 3.7 km/s mentioned above. Though this fast-propagating rupture

is not observed in the SEBP analysis, the FFI and SEBP results are not conflicting since the BP images before 20 s might be affected by the signal interference between two fronts (Figures 6d–6k). Thus, we suspect that the super-shear ruptures, if any, should be local and likely to occur on some portions of the east rupture before or around the 20 s.

Previously, two super-shear earthquakes (the 2001 Mw 7.8 Kunlun and the 2010 Mw 6.9 Yushu) occurred on the boundary faults of the Bayan Har block. According to interseismic GNSS velocity data (M. Wang & Shen, 2020), greater tangential velocity gradients across the boundary faults are observed than in the block's interior (M. Wang et al., 2022b), which induces larger long-term slip rates on the block boundaries. Large slip rates lead to smoother and more structurally mature faults, one major condition for super-shear rupture (Perrin et al., 2016). Unlike these two events, the 2021 Maduo earthquake occurred on the intra-block and less-mature Kunlun Pass-Jiangcuo fault. The lack of sufficiently long and smooth fault segments may be one contributor to the overall sub-shear rupture speeds. However, this condition does not exclude the possibility of local super-shear speeds because small-scale heterogeneities on the fault can lead to variations in the rupture speed (Spudich & Frazer, 1984).

#### 4.4. Constraint on the Slip Partition From SAR Azimuth Displacement

With a strike of  $\sim 106^\circ$ , the static displacement of the Maduo earthquake is primarily oriented in the E-W direction. However, the eastern fault bifurcation introduces the large fault-normal displacement in the N-S direction (Figure S2 in Supporting Information S1), which is only measurable using the azimuth offsets due to the limited diversity of line-of-sight orientations of polar-orbiting SAR satellites. Most previous studies use only the static displacement in the range direction from InSAR or speckle tracking (K. Chen et al., 2022; Hong et al., 2022; Jin & Fialko, 2021; Q. Li et al., 2022b; Zhang et al., 2022). J. Liu et al. (2022a) use the burst overlap interferometry to obtain spatially sparse azimuth displacements, while Lyu et al. (2022) use speckle tracking to obtain continuous azimuth displacements with low SNR. We adopt extra procedures (Section 2.2) on top of speckle tracking to obtain a spatially continuous azimuth offset with high SNR at the cost of reduced spatial resolution (Figure S3 in Supporting Information S1).

To see how the azimuth offset data improve the inversion, we perform an additional inversion without the azimuth offsets and compare the result with the preferred model (Figures 7a and 7c). With the azimuth displacement data included, the maximum slip on the East segment decreases from 5.9 to 4.9 m, while the average slip around the junction (magenta boxes in Figure 7c) on the Middle segment increases from 2.8 to 3.1 m. Another distinct difference is that the shallow slip of the East segment near the fault junction (red boxes in Figure 7c) decreases from 3 to 1 m when including azimuth offsets. The smaller shallow slip indicates that the rupture steps onto the East segment through the deep ( $>2$  km) rather than the near-surface portion ( $<2$  km) of the fault. The involvement of azimuth offsets in the FFI of the Maduo earthquake demonstrates that for earthquakes rupturing complex fault systems, the inversion should include the static deformation data in both range and azimuth directions to better constrain the slip distribution.

#### 4.5. Static CFS Change and the Rupture Bifurcation

W. Wang et al. (2021) performed a relocation study for the aftershocks of the Mw 7.4 Maduo earthquake. They relocated 1199  $M > 0$  aftershocks within 8 days after the mainshock. We shift the relocated aftershocks horizontally to our fault planes (Figure 7a) and find that the aftershocks are noticeably less common in the principal-slip area (purple hollow ellipses in Figure 7a). On the other hand, we observe dense aftershocks at the edges of large-slip patches (yellow hollow ellipses in Figure 7a), which is a common feature of many large earthquakes (Kato & Igarashi, 2012; Kato et al., 2010; Mendoza & Hartzell, 1988). The decoupling of large-slip and aftershocks suggests that the asperities with large coseismic slips are probably locked in the post-seismic period and could be explained by the static CFS change ( $\Delta$ CFS, Figure 7d). We calculate the CFS change on the left-lateral strike-slip fault surface using Coulomb 3 (King et al., 1994; Toda et al., 2011). On the fault planes, much more aftershocks are located in the CFS-increasing areas (yellow hollow ellipses in Figure 7d) than in the CFS-decreasing areas (purple hollow ellipses). The coseismic slip increases the CFS at the edge of the large-slip zones and casts the negative  $\Delta$ CFS, which prohibits the aftershocks, on these large-slip zones.

The range offset map (Figure 2b) and the aftershock locations (Figure 8 of W. Wang et al., 2021) reveal that the Kunlun Pass-Jiangcuo fault bifurcates at the eastern end during the Maduo earthquake. According to the surface deformation pattern, the rupture propagates on the main fault (Middle segment) and the branching fault (East segment). According to its orientation and left-lateral motion, the branching fault is on the extensional side. Rupture bifurcation is a complicated issue investigated by theoretical and numerical studies. During the 2001 Mw 7.8 Kunlun earthquake, a

fault bifurcation near the Kunlun Pass fault might be responsible for slowing down the rupture (Robinson et al., 2006). Kame and Yamashita (1999a, 1999b) showed that the dynamic growth of a rupture tends to be arrested soon after the bifurcation because the stress concentration at the rupture tip is reduced after the bifurcation. According to the rupture dynamic simulation studies (Bhat et al., 2004; Kame et al., 2003), whether rupture can continue beyond the bifurcation point depends on the inclination of the maximum pre-compression ( $S_{\max}$ ), the rupture velocity ( $V_r$ ), and the branching angle ( $\theta$ , angles between the primary and branching fault).

We find the Kame et al. (2003) simulation results applicable in understanding the features associated with the east-end bifurcation of the Maduo earthquake. Figure 2b shows that at the eastern fork, the inclination of  $S_{\max}$  is  $\sim 43^\circ$  (intermediate inclination) according to the GNSS velocity field (M. Wang et al., 2022b) and fault geometry, with a branching angle  $\theta$  of  $\sim 23^\circ$ . The direction of the maximum shear strain rate agrees well with the strike direction of the Kunlun Pass-Jiangcuo Fault (M. Wang et al., 2022b), on which the Middle segment locates. For mode II rupture governed by the slip-weakening law, the orientation of the most favored rupture plane is close to the strike of the main fault, while the shear stress could exceed the frictional resistance on the faults branching out the main fault plane up to  $30^\circ$  (Kame et al., 2003). Kame et al. (2003) dynamic simulation showed that under the intermediate inclination of  $S_{\max}$ , the failure on the main fault is dynamically self-chosen, and simultaneous rupture on both the main fault and branching fault is possible. Meanwhile, the BP-inferred  $V_r$  is  $\sim 3$  km ( $\sim 0.8$  Vs), which is fast enough and causes high dynamic stressing to drive the rupture after bifurcation on both faults. The wide branching angle  $\theta$  makes rupture on both faults less affected by stress interaction, thus reducing the stress shadow effect (the stress release around one fault discourages the failure on vicinity faults).

## 5. Summary and Conclusions

We conduct joint FFI and SEBP analysis to explore the kinematic rupture history of the 21 May 2021 Mw 7.4 Maduo, Tibet earthquake with 3D ground displacements from radar satellites, broadband body waves, and long-period surface waves recorded at teleseismic distances. This earthquake is a left-lateral strike-slip rupture that initiates in the middle of a 160 km long north-dipping sub-vertical fault system and propagates bilaterally. The cumulative seismic moment is  $1.83 \times 10^{20}$  Nm, yielding a moment magnitude of 7.44. About 95% of the total seismic moment occurs in the first 32 s. By jointly analyzing multiple data sets, we find.

1. 77% of the total seismic moment occurs on the asperities shallower than 10 km with a peak slip of 5.7 m. Similar to previous results (Hong et al., 2022; Jin & Fialko, 2021), our model shows a significant shallow slip deficit in the top 2 km, where the along-strike average slip reduces by 43% from 3.2 to 1.8 m.
2. Possible deep slip appears below 10 km depth to simultaneously explain the observed long-period seismic waves and static displacements. Tests show a tradeoff between the inverted deep slip magnitude and the rigidity of the crustal model in the shallow depths. The existence and amount of possible deep slip in the middle crust deserves further investigation.
3. Both SEBP and FFI studies suggest an overall sub-shear rupture, breaking the west branch of 75 km at 2.7 km/s and the east branch of 85 km at 3.0 km/s. Super-shear ruptures possibly occur in some parts of the east propagation as reported by several studies adopting MTW FFI and BP methods (e.g., K. Chen et al., 2022; Lyu et al., 2022; Yue et al., 2022; Zhang et al., 2022). Our synthetic tests confirm overall sub-shear rupture speeds but also show that super-shear ruptures in SEBP analysis might be obscured by signal interference between bilateral branches.
4. The aftershock distribution on the fault plane is consistent with positive  $\Delta CFS$  zones and forms a complementary pattern to the coseismic slip areas.
5. The fault surface trace indicates a bifurcation near the eastern terminal end of the rupture. Including the azimuth offsets derived from SAR images improves the constraint on the slip partition on splay faults. The branching behaviors agree with the previous dynamic simulation results (e.g., Kame et al., 2003). The fast rupture speed and the intermediate inclination of maximum compression promote the rupture on the branching and main faults. The wide angle between these faults reduces the stress shadow effect.

## Data Availability Statement

The Copernicus Sentinel-1 data are provided by ESA and obtained from the Alaska Satellite Facility (<https://search.asf.alaska.edu/>). The InSAR Scientific Computing Environment (ISCE) software is available at <https://github.com/isce-framework/isce2>. The SAR/InSAR processing recipe and products are available at

<https://doi.org/10.5281/zenodo.7141135> and <https://doi.org/10.5281/zenodo.7170329>. The slip model and SEBP results are available at <https://doi.org/10.5281/zenodo.7761908>. The moment tensor solutions come from the U.S. Geological Survey (USGS; <http://earthquake.usgs.gov>) and the Global Centroid Moment Tensor project (CMT; <http://www.globalcmt.org>). The MATLAB code of SEBP is available at <https://github.com/lsmeng/MUSICBP/tree/SEBP>. All seismic data are downloaded through the IRIS Wilber 3 system (<https://ds.iris.edu/wilber3/>) and ORFEUS ([www.orfeus-eu.org](http://www.orfeus-eu.org)), including the following seismic networks: (a) the TA (Transportable Array; IRIS, 2003); (b) the US (USNSN, Albuquerque, 1990); (c) the IU (GSN; Albuquerque, 1988); (d) the CZ (Czech Regional Seismic Network, Czech, 1973); (e) the EI (Dublin Institute for Advanced Studies, 1993); (f) the GR (Federal Institute for Geosciences and Natural Resources, 1976); (g) the GU (University of Genoa, 1967); (h) the IV (INGV Seismological Data Centre, 2006); (i) the MN (MedNet Project Partner Institutions, 1990); (j) the NL (KNMI, 1993); (k) the OE (ZAMG, 1987); (l) the OX (OGS, 2016); (m) the TH (Institut fuer Geowissenschaften, Friedrich-Schiller-Universitaet Jena, 2009); (n) the AK (Alaska Earthquake Center, Univ. of Alaska Fairbanks, 1987); (o) the AV (Alaska Volcano Observatory/USGS, 1988); (p) the AT (NOAA, USA, 1967); (q) the II (Scripps Institution of Oceanography, 1986); (r) the AU (Australian National Seismograph Network Data Collection, Canberra, 2011); (s) the G (IPGP and EOST, 1982); (t) the GE (GEOFON Data Centre, 1993); (u) the ND (Centre IRD de Noumea, Nouvelle-Caledonie, 2010); (v) the S1 (ANU, Australia, 2011); (w) the FR (RESIF, 1995); (x) the DK, EE, FN, MY, PS, SI. The relocated aftershock data is from Wang et al. (2021). The USTClitho2.0 model is from Han et al. (2021). The velocity model of northeast Tibet is from Xia et al. (2021). The Python software package Obspy ([www.obspy.org](http://www.obspy.org)) is used for seismic data requesting, waveform filtering, and cross-correlation processing. Figures are produced using Generic Mapping Tools (GMT), Matlab, Matplotlib, and Cartopy. The static displacement data is downsampled by InSamp (<https://github.com/williamBarnhart/InSamp>).

## Acknowledgments

The authors appreciate the insightful comments from two anonymous reviewers, associate editor, and editor Rachel Abercrombie, which have greatly improved the manuscript. The authors thank Lei Shi for sharing the velocity model of northeast Tibet, Weilai Wang for sharing the aftershock catalog, and Zeyu Jin, Shunyong Hong, Caijun Xu, and Qi Li for sharing their slip models, Dijin Wang and Kejie Chen for sharing the GNSS data. The authors thank Zeyu Jin, Jiuxun Yin, and Rishav Mallick for fruitful discussions. This work contains modified Copernicus data from the Sentinel-1A and -1B satellites provided by the European Space Agency (ESA). This work is supported by the NSF CAREER grant (EAR-1848486) and the Leon and Joanne V.C. Knopoff Fund. Chen Ji is supported by grants from the Southern California Earthquake Center (SCEC)-funded by NSF cooperative agreement EAR-0109624 and USGS cooperative agreement 02HQAG0008. Part of this research is performed at the Jet Propulsion Laboratory, California Institute of Technology under contract with the National Aeronautics and Space Administration (80NM0018D0004) and supported by the Earth Surface and Interior focus area.

## References

- Aderhold, K., & Abercrombie, R. E. (2016). Seismotectonics of a diffuse plate boundary: Observations off the Sumatra-Andaman trench. *Journal of Geophysical Research: Solid Earth*, 121, 3462–3478. <https://doi.org/10.1002/2015JB012721>
- Alaska Earthquake Center, University of Alaska Fairbanks. (1987). Alaska Regional Network [Dataset]. International Federation of Digital Seismograph Networks. <https://doi.org/10.7914/SN/AK>
- Alaska Volcano Observatory/USGS. (1988). Alaska Volcano Observatory [Dataset]. International Federation of Digital Seismograph Networks. <https://doi.org/10.7914/SN/AV>
- Albuquerque Seismological Laboratory (ASL)/USGS. (1988). Global Seismograph Network (GSN - IRIS/USGS). *International Federation of Digital Seismograph Networks*. <https://doi.org/10.7914/SN/IU>
- Albuquerque Seismological Laboratory (ASL)/USGS. (1990). United States National Seismic Network. International Federation of Digital Seismograph Networks. <https://doi.org/10.7914/SN/US>
- Australian National University (ANU, Australia). (2011). Australian Seismometers in Schools [Dataset]. International Federation of Digital Seismograph Networks. <https://doi.org/10.7914/SN/S1>
- Bao, H., Ampuero, J. P., Meng, L., Fielding, E. J., Liang, C., Feng, T., & Huang, H. (2019). Early and persistent supershear rupture of the 2018 Mw 7.5 Palu earthquake. *Nature Geoscience*, 12(3), 200–205. <https://doi.org/10.1038/s41561-018-0297-z>
- Bhat, H. S., Dmowska, R., Rice, J. R., & Kame, N. (2004). Dynamic slip transfer from the Denali to Totschunda Faults, Alaska: Testing theory for fault branching. *Bulletin of the Seismological Society of America*, 94(6B), S202–S213. <https://doi.org/10.1785/0120040601>
- Brocher, T. M. (2005). Empirical relations between elastic wavespeeds and density in the Earth's crust. *Bulletin of the Seismological Society of America*, 95(6), 2081–2092. <https://doi.org/10.1785/0120050077>
- Centre IRD de Noumea, Nouvelle-Caledonie. (2010). New Caldonia Broadband Seismic Network [Dataset]. International Federation of Digital Seismograph Networks. <https://doi.org/10.7914/SN/ND>
- Charles University in Prague (Czech), Institute of Geonics, Institute of Geophysics, Academy of Sciences of the Czech Republic, Institute of Physics of the Earth Masaryk University (Czech), & Institute of Rock Structure and Mechanics. (1973). Czech Regional Seismic Network [Dataset]. International Federation of Digital Seismograph Networks. <https://doi.org/10.7914/SN/CZ>
- Chen, C. W., & Zebker, H. A. (2001). Two-dimensional phase unwrapping with use of statistical models for cost functions in nonlinear optimization. *Journal of the Optical Society of America A*, 18(2), 338–351. <https://doi.org/10.1364/JOSAA.18.000338>
- Chen, K., Avouac, J.-P., Geng, J., Liang, C., Zhang, Z., Li, Z., & Zhang, S. (2022). The 2021 Mw 7.4 Maoji earthquake: An archetype bilateral slip-pulse rupture arrested at a splay fault. *Geophysical Research Letters*, 49(2), e2021GL095243. <https://doi.org/10.1029/2021GL095243>
- Dahlen, F. A., & Tromp, J. (1999). *Theoretical global seismology*. Princeton University Press. <https://doi.org/10.1515/9780691216157>
- Day, S. M. (1982). Three-dimensional finite difference simulation of fault dynamics: Rectangular faults with fixed rupture velocity. *Bulletin of the Seismological Society of America*, 72, 705–727.
- Deng, Q. (2007). *Active Tectonic Map of China (1:400 million)*. Earthquake Press. ISBN 10: 7502830510
- De Zan, F. (2014). Accuracy of incoherent speckle tracking for circular Gaussian signals. *IEEE Geoscience and Remote Sensing Letters*, 11(1), 264–267. <https://doi.org/10.1109/LGRS.2013.2255259>
- Du, H. (2021). Estimating rupture front of large earthquakes using a novel multi-array back-projection method. *Frontiers of Earth Science*, 9, <https://doi.org/10.3389/feart.2021.680163>
- Dublin Institute for Advanced Studies. (1993). Irish National Seismic Network [Dataset]. International Federation of Digital Seismograph Networks. <https://doi.org/10.7914/SN/EI>
- Dziewonski, A. M., & Anderson, D. L. (1981). Preliminary reference Earth model. *Physics of the Earth and Planetary Interiors*, 25(4), 297–356. [https://doi.org/10.1016/0031-9201\(81\)90046-7](https://doi.org/10.1016/0031-9201(81)90046-7)

- Fattah, H., Agram, P., & Simons, M. (2017). A network-based enhanced spectral diversity approach for TOPS time-series analysis. *IEEE Transactions on Geoscience and Remote Sensing*, 55(2), 777–786. <https://doi.org/10.1109/TGRS.2016.2614925>
- Federal Institute for Geosciences Natural Resources. (1976). German Regional Seismic Network (GRSN). Other/Seismic Network. <https://doi.org/10.25928/mbx6-hr74>
- Fialko, Y., Simons, M., & Agnew, D. (2001). The complete (3-D) surface displacement field in the epicentral area of the 1999 Mw 7.1 Hector Mine earthquake, California, from space geodetic observations. *Geophysical Research Letters*, 28(16), 3063–3066. <https://doi.org/10.1029/2001GL013174>
- Fielding, E. J., Liu, Z., Stephenson, O. L., Zhong, M., Liang, C., Moore, A., et al. (2020). Surface deformation related to the 2019 Mw 7.1 and Mw 6.4 Ridgecrest earthquakes in California from GPS, SAR interferometry, and SAR pixel offsets. *Seismological Research Letters*, 91(4), 2035–2046. <https://doi.org/10.1785/0220190302>
- Gardner, G. H. F., Gardner, L. W., & Gregory, A. R. (1974). Formation velocity and density—The diagnostic basics for stratigraphic traps. *Geophysics*, 39(6), 770–780. <https://doi.org/10.1190/1.1440465>
- GEOFON Data Centre. (1993). GEOFON seismic network. GFZ Data Services. Other/Seismic Network. <https://doi.org/10.14470/TR560404>
- Gisinger, C., Schubert, A., Breit, H., Garthwaite, M., Balss, U., Willberg, M., et al. (2021). In-depth verification of Sentinel-1 and TerraSAR-X geolocation accuracy using the Australian corner reflector array. *IEEE Transactions on Geoscience and Remote Sensing*, 59(2), 1154–1181. <https://doi.org/10.1109/TGRS.2019.2961248>
- Han, S., Zhang, H., Xin, H., Shen, W., & Yao, H. (2021). USTC litho2.0: Updated unified seismic tomography models for continental China lithosphere from joint inversion of body-wave arrival times and surface-wave dispersion data. *Seismological Research Letters*, 93(1), 201–215. <https://doi.org/10.1785/0220210122>
- Hartzell, S. H., & Heaton, T. H. (1983). Inversion of strong ground motion and teleseismic waveform data for the fault rupture history of the 1979 Imperial Valley, California, earthquake. *Bulletin of the Seismological Society of America*, 73(6A), 1553–1583. <https://doi.org/10.1785/BSSA07306A1553>
- Hartzell, S. H., Liu, P., & Mendoza, C. (1996). The 1994 Northridge, California, earthquake: Investigation of rupture velocity, rise time, and high-frequency radiation. *Journal of Geophysical Research B: Solid Earth*, 101(9), 20091–20108. <https://doi.org/10.1029/96jb01883>
- Hersbach, H., Bell, B., Berrisford, P., Hirahara, S., Horányi, A., Muñoz-Sabater, J., et al. (2020). The ERA5 global reanalysis. *Quarterly Journal of the Royal Meteorological Society*, 146(730), 1999–2049. <https://doi.org/10.1002/qj.3803>
- Hong, S., Liu, M., Liu, T., Dong, Y., Chen, L., Meng, G., & Xu, Y. (2022). Fault source model and stress changes of the 2021 Mw 7.4 Maduo earthquake, China, constrained by InSAR and GPS measurements. *Bulletin of the Seismological Society of America*. <https://doi.org/10.1785/0120210250>
- INGV Seismological Data Centre. (2006). Rete Sismica Nazionale (RSN). Istituto Nazionale di Geofisica e Vulcanologia (INGV). <https://doi.org/10.13127/SD/X0FXNH7QFY>
- Institut de Physique du Globe de Paris (IPGP) and Ecole et Observatoire des Sciences de la Terre de Strasbourg (EOST). (1982). GEOSCOPE, French global network of broad band seismic stations. Institut de Physique du Globe de Paris (IPGP). <https://doi.org/10.18715/GEOSCOPE.G>
- Institut fuer Geowissenschaften, Friedrich-Schiller-Universitaet Jena. (2009). Thüringer Seismologisches Netz [Dataset]. International Federation of Digital Seismograph Networks. <https://doi.org/10.7914/SN/TH>
- IRIS Transportable Array. (2003). USArray Transportable Array. International Federation of Digital Seismograph Networks. <https://doi.org/10.7914/SN/TA>
- Ishii, M., Shearer, P. M., Houston, H., & Vidale, J. E. (2005). Extent, duration, and speed of the 2004 Sumatra-Andaman earthquake imaged by the Hi-Net array. *Nature*, 435(7044), 933–936. <https://doi.org/10.1038/nature03675>
- Istituto Nazionale di Oceanografia e di Geofisica Sperimentale—OGS (2016). North-East Italy Seismic Network [Dataset]. FDSN. <https://doi.org/10.7914/SN/OX>
- Ji, C., Helmberger, D. V., Wald, D. J., & Ma, K.-F. (2003). Slip history and dynamic implications of the 1999 Chi-Chi, Taiwan, earthquake. *Journal of Geophysical Research*, 108, 2412. <https://doi.org/10.1029/2002JB001764>
- Ji, C., Wald, D. J., & Helmberger, D. V. (2002). Source description of the 1999 Hector Mine, California, earthquake, Part I: Wavelet domain inversion theory and resolution analysis. *Bulletin of the Seismological Society of America*, 92(4), 1192–1207. <https://doi.org/10.1785/0120000916>
- Jin, Z., & Fialko, Y. (2021). Coseismic and early postseismic deformation due to the 2021 M7.4 Maduo (China) earthquake. *Geophysical Research Letters*, 48(21), e2021GL095213. <https://doi.org/10.1029/2021GL095213>
- Jolivet, R., Grandin, R., Lasserre, C., Doin, M. P., & Peltzer, G. (2011). Systematic InSAR tropospheric phase delay corrections from global meteorological reanalysis data. *Geophysical Research Letters*, 38(17), L17311. <https://doi.org/10.1029/2011GL048757>
- Kame, N., Rice, J., & Dmowska, R. (2003). Effects of prestress state and rupture velocity on dynamic fault branching. *Journal of Geophysical Research*, 108(B5). <https://doi.org/10.1029/2002JB002189>
- Kame, N., & Yamashita, T. (1999a). A new light on arresting mechanism of dynamic earthquake faulting. *Geophysical Research Letters*, 26(13), 1997–2000. <https://doi.org/10.1029/1999GL900410>
- Kame, N., & Yamashita, T. (1999b). Simulation of the spontaneous growth of a dynamic crack without constraints on the crack tip path. *Geophysical Journal International*, 139(2), 345–358. <https://doi.org/10.1046/j.1365-246X.1999.00940.x>
- Kanamori, H., & Given, J. W. (1981). Use of long-period surface waves for rapid determination of earthquake-source parameters. *Physics of the Earth and Planetary Interiors*, 27(1), 8–31. [https://doi.org/10.1016/0031-9201\(81\)90083-2](https://doi.org/10.1016/0031-9201(81)90083-2)
- Kato, A., & Igarashi, T. (2012). Regional extent of the large coseismic slip zone of the 2011 Mw 9.0 Tohoku-Oki earthquake delineated by on-fault aftershocks. *Geophysical Research Letters*, 39(15), 15301. <https://doi.org/10.1029/2012GL052220>
- Kato, A., Miyatake, T., & Hirata, N. (2010). Asperity and barriers of the 2004 Mid-Niigata Prefecture earthquake revealed by highly dense seismic observations. *Bulletin of the Seismological Society of America*, 100(1), 298–306. <https://doi.org/10.1785/0120090218>
- Kennett, B. L. N., & Engdahl, E. R. (1991). Travel times for global earthquake location and phase identification. *Geophysical Journal International*, 105(2), 429–465. <https://doi.org/10.1111/j.1365-246X.1991.tb06724.x>
- Kind, R., Yuan, X., Saul, J., Nelson, D., Sobolev, S. V., Mechie, J., et al. (2002). Seismic images of crust and upper mantle beneath Tibet: Evidence for Eurasian plate subduction. *Science*, 298(5596), 1219–1221. <https://doi.org/10.1126/science.1078115>
- King, G., Stein, R., & Lin, J. (1994). Static stress changes and the triggering of earthquakes. *Bulletin of the Seismological Society of America*, 84 (3), 935–953. <https://doi.org/10.1785/BSSA0840030935>
- Kiser, E., & Ishii, M. (2017). Back-projection imaging of earthquakes. *Annual Review of Earth and Planetary Sciences*, 45(1), 271–299. <https://doi.org/10.1146/annurev-earth-063016-015801>
- KNMI. (1993). Netherlands seismic and acoustic network. Royal Netherlands Meteorological Institute (KNMI). Other/Seismic Network. <https://doi.org/10.21944/e970fd34-23b9-3411-b366-e4f72877d2c5>

- Langston, C. A., & Helmberger, D. V. (1975). A procedure for modeling shallow dislocation sources. *Geophysical Journal International*, 42(1), 117–130. <https://doi.org/10.1111/j.1365-246X.1975.tb05854.x>
- Li, B., Wu, B., Bao, H., Oglesby, D. D., Ghosh, A., Gabriel, A.-A., et al. (2022a). Rupture heterogeneity and directivity effects in back-projection analysis. *Journal of Geophysical Research: Solid Earth*, 127(3), e2021JB022663. <https://doi.org/10.1029/2021JB022663>
- Li, Q., Wan, Y., Li, C., Tang, H., Tan, K., & Wang, D. (2022b). Source process featuring asymmetric rupture velocities of the 2021 Mw 7.4 Maduo, China, earthquake from teleseismic and geodetic data. *Seismological Research Letters*, 93(3), 1429–1439. <https://doi.org/10.1785/0220210300>
- Liu, J., Hu, J., Li, Z., Ma, Z., Wu, L., Jiang, W., et al. (2022a). Complete three-dimensional coseismic displacements due to the 2021 Maduo earthquake in Qinghai Province, China from Sentinel-1 and ALOS-2 SAR images. *Science China Earth Sciences*, 65(1674–7313), 687–697. <https://doi.org/10.1007/s11430-021-9868-9>
- Liu, X., Chen, Q., Yang, Y., Xu, Q., Zhao, J., Xu, L., & Liu, R. (2022b). The 2021 Mw 7.4 Maduo earthquake: Coseismic slip model, triggering effect of historical earthquakes and implications for adjacent fault rupture potential. *Journal of Geodynamics*, 151, 101920. <https://doi.org/10.1016/j.jog.2022.101920>
- Liu, Z., Tian, X., Liang, X., Liang, C., & Li, X. (2021). Magmatic underplating thickening of the crust of the southern Tibetan Plateau inferred from receiver function analysis. *Geophysical Research Letters*, 48(17), e2021GL093754. <https://doi.org/10.1029/2021GL093754>
- Lohman, R. B., & Barnhart, W. D. (2010). Evaluation of earthquake triggering during the 2005–2008 earthquake sequence on Qeshm Island, Iran. *Journal of Geophysical Research*, 115(B12), B12413. <https://doi.org/10.1029/2010JB007710>
- Lohman, R. B., & Simons, M. (2005). Some thoughts on the use of InSAR data to constrain models of surface deformation: Noise structure and data downsampling. *Geochemistry, Geophysics, Geosystems*, 6(1), Q01007. <https://doi.org/10.1029/2004GC000841>
- Lyu, M., Chen, K., Xue, C., Zang, N., Zhang, W., & Wei, G. (2022). Overall subshear but locally supershear rupture of the 2021 Mw 7.4 Maduo earthquake from high-rate GNSS waveforms and three-dimensional InSAR deformation. *Tectonophysics*, 839, 229542. <https://doi.org/10.1016/j.tecto.2022.229542>
- MedNet Project Partner Institutions. (1990). *Mediterranean Very Broadband Seismographic Network (MedNet)*. Istituto Nazionale di Geofisica e Vulcanologia (INGV). <https://doi.org/10.13127/SD/FBBTDTD6Q>
- Mendoza, C., & Hartzell, S. H. (1988). Aftershock patterns and main shock faulting. *Bulletin of the Seismological Society of America*, 78(4), 1438–1449. <https://doi.org/10.1785/BSSA0780041438>
- Meng, L., Ampuero, J.-P., Stock, J., Duputel, Z., Luo, Y., & Tsai, V. C. (2012). Earthquake in a Maze: Compressional rupture branching during the 2012 Mw 8.6 Sumatra Earthquake. *Science*, 337(6095), 724–726. <https://doi.org/10.1126/science.1224030>
- Meng, L., Bao, H., Huang, H., Zhang, A., Bloore, A., & Liu, Z. (2018). Double pincer movement: Encircling rupture splitting during the 2015 Mw 8.3 Illapel earthquake. *Earth and Planetary Science Letters*, 495, 164–173. <https://doi.org/10.1016/j.epsl.2018.04.057>
- Meng, L., Huang, H., Xie, Y., Bao, H., & Dominguez, L. A. (2019). Nucleation and kinematic rupture of the 2017 Mw 8.2 Tehuantepec earthquake. *Geophysical Research Letters*, 46(7), 3745–3754. <https://doi.org/10.1029/2018GL081074>
- Meng, L., Inbal, A., & Ampuero, J.-P. (2011). A window into the complexity of the dynamic rupture of the 2011 Mw 9 Tohoku-Oki earthquake. *Geophysical Research Letters*, 38(7), L00G07. <https://doi.org/10.1029/2011GL048118>
- Meng, L., Zhang, A., & Yagi, Y. (2016). Improving back projection imaging with a novel physics-based aftershock calibration approach: A case study of the 2015 Gorkha earthquake. *Geophysical Research Letters*, 43(2), 628–636. <https://doi.org/10.1002/2015GL067034>
- Michel, R., Avouac, J.-P., & Taboury, J. (1999). Measuring ground displacements from SAR amplitude images: Application to the Landers earthquake. *Geophysical Research Letters*, 26(7), 875–878. <https://doi.org/10.1029/1999GL900138>
- NOAA National Oceanic and Atmospheric Administration (USA). (1967). National Tsunami Warning Center Alaska Seismic Network [Dataset]. International Federation of Digital Seismograph Networks. <https://doi.org/10.7914/SN/AT>
- Oliver-Cabrera, T., Jones, C. E., Yunjun, Z., & Simard, M. (2021). InSAR phase unwrapping error correction for rapid repeat measurements of water level change in wetlands. *IEEE Transactions on Geoscience and Remote Sensing*, 60, 1–15. <https://doi.org/10.1109/TGRS.2021.3108751>
- Perrin, C., Manighetti, I., Ampuero, J.-P., Cappa, F., & Gaudemer, Y. (2016). Location of largest earthquake slip and fast rupture controlled by along-strike change in fault structural maturity due to fault growth. *Journal of Geophysical Research: Solid Earth*, 121(5), 3666–3685. <https://doi.org/10.1002/2015JB012671>
- RESIF. (1995). *RESIF-RBTP French Broad-band network, RESIF-RAP strong motion network and other seismic stations in metropolitan France*. RESIF—Réseau Sismologique et Géodésique Français. <https://doi.org/10.15778/resif.fr>
- Robinson, D. P., Brough, C., & Das, S. (2006). The Mw 7.8, 2001 Kunlunshan earthquake: Extreme rupture speed variability and effect of fault geometry. *Journal of Geophysical Research*, 111(B8), B08303. <https://doi.org/10.1029/2005JB004137>
- Rosen, P. A., Gurrola, E., Sacco, G. F., & Zebker, H. (2012). The InSAR scientific computing environment. Paper presented at the EUSAR 2012. Scripps Institution of Oceanography. (1986). Global Seismograph Network - IRIS/IDA [Dataset]. International Federation of Digital Seismograph Networks. <https://doi.org/10.7914/SN/II>
- Sen, M. K., & Stoffa, P. L. (1991). Nonlinear one-dimensional seismic waveform inversion using simulated annealing. *GEOPHYSICS*, 56(10), 1624–1638. <https://doi.org/10.1190/1.1442973>
- Spudich, P., & Frazer, L. (1984). Use of ray theory to calculate high-frequency radiation from earthquake sources having spatially variable rupture velocity and stress drop. *Bulletin of the Seismological Society of America*, 74(6), 2061–2082. <https://doi.org/10.1785/BSSA0740062061>
- Tinti, E., Fukuyama, E., Piatanesi, A., & Cocco, M. (2005). A kinematic source-time function compatible with earthquake dynamics. *Bulletin of the Seismological Society of America*, 95(4), 1211–1223. <https://doi.org/10.1785/0120040177>
- Toda, S., Stein, R. S., Sevilgen, V., & Lin, J. (2011). Coulomb 3.3 Graphic-rich deformation and stress-change software for earthquake, tectonic, and volcano research and teaching—User guide (p. 63). U.S. Geological Survey Open-File Report 2011–1060. Retrieved from <https://pubs.usgs.gov/of/2011/1060/>
- University of Genoa. (1967). Regional Seismic Network of North Western Italy [Dataset]. International Federation of Digital Seismograph Networks. <https://doi.org/10.7914/SN/GU>
- USGS. (2022). Retrieved from <https://earthquake.usgs.gov/earthquakes/eventpage/us7000e54r/moment-tensor>
- Vallée, M., & Dunham, E. M. (2012). Observation of far-field Mach waves generated by the 2001 Kokoxili supershear earthquake. *Geophysical Research Letters*, 39(5), L05311. <https://doi.org/10.1029/2011GL050725>
- Waldhauser, F., & Ellsworth, W. (2000). A double-difference earthquake location algorithm: Method and application to the Northern Hayward Fault, California. *Bulletin of the Seismological Society of America*, 90(6), 1353–1368. <https://doi.org/10.1785/0120000006>
- Wang, D., Wang, D., Zhao, B., Li, Y., Zhao, L., Wang, Y., et al. (2022a). 2021 Mw 7.4 Maduo earthquake co-seismic deformation field and slip distribution using GNSS observations. *Geophysical Journal of China*, 65(2), 537–551. <https://doi.org/10.6038/cjg2022P0568>
- Wang, M., & Shen, Z. K. (2020). Present-day crustal deformation of continental China derived from GPS and its tectonic implications. *Journal of Geophysical Research*, 125(2), e2019JB018774. <https://doi.org/10.1029/2019JB018774>

- Wang, M., Wang, F., Jiang, X., Tian, J., Li, Y., Sun, J., & Shen, Z. (2022b). GPS determined coseismic slip of the 2021 Mw7.4 Maduo, China, earthquake and its tectonic implication. *Geophysical Journal International*, 228(3), 2048–2055. <https://doi.org/10.1093/gji/ggab460>
- Wang, W., Fang, L., Wu, J., Tu, H., Chen, L., Lai, G., & Zhang, L. (2021). Aftershock sequence relocation of the 2021 MS7.4 Maduo earthquake, Qinghai, China. *Science China Earth Sciences*, 64(8), 1371–1380. (in Chinese). <https://doi.org/10.1007/s11430-021-9803-3>
- Wang, W., He, J., Wang, X., Zhou, Y., Hao, J., Zhao, L., & Yao, Z. (2022c). Rupture process models of the Yangbi and Maduo earthquakes that struck the eastern Tibetan Plateau in May 2021. *Science Bulletin*, 67(5), 466–469. <https://doi.org/10.1016/j.scib.2021.11.009>
- Wen, Y., Ma, K., Song, T. A., & Mooney, W. D. (2009). Validation of the rupture properties of the 2001 Kunlun, China (Ms = 8.1), earthquake from seismological and geological observations. *Geophysical Journal International*, 177(2), 555–570. <https://doi.org/10.1111/j.1365-246X.2008.04063.x>
- Wu, S., Li, G., He, F., Zhang, Y., Shi, S., Han, J., & Zeng, L. (2002). Geometry and kinematics in the east segment of the surface rupture zone occurring during the Kunlun earthquake. *Geological Bulletin of China*, 21, 8–9. <https://doi.org/10.1080/12265080208422884>
- Xia, S., Shi, L., Li, Y., & Guo, L. (2021). Velocity structures of the crust and uppermost mantle beneath the northeastern margin of Tibetan Plateau revealed by double-difference tomography. *Chinese Journal of Geophysics*, 64(9), 3194–3206. <https://doi.org/10.6038/cjg202100514>
- Yao, H., Gerstoft, P., Shearer, P. M., & Mecklenbräuker, C. (2011). Compressive sensing of the Tohoku-Oki Mw 9.0 earthquake: Frequency-dependent rupture modes. *Geophysical Research Letters*, 38(20), L20310. <https://doi.org/10.1029/2011GL049223>
- Yoffe, E. H. (1951). LXXV. The moving Griffith crack. *The London, Edinburgh and Dublin Philosophical Magazine and Journal of Science*, 42(330), 739–750. <https://doi.org/10.1080/14786445108561302>
- Yokota, Y., Kawazoe, Y., Yun, S., Oki, S., Aoki, Y., & Koketsu, K. (2012). Joint inversion of teleseismic and InSAR data sets for the rupture process of the 2010 Yushu, China, earthquake. *Earth, Planets, and Space*, 64(11), 1047–1051. <https://doi.org/10.5047/eps.2012.04.008>
- Yue, H., Shen, Z.-K., Zhao, Z., Wang, T., Cao, B., Li, Z., et al. (2022). Rupture process of the 2021 M7.4 Maduo earthquake and implication for deformation mode of the Songpan-Ganzi terrane in Tibetan Plateau. *Proceedings of the National Academy of Sciences*, 119(23), e2116445119. <https://doi.org/10.1073/pnas.2116445119>
- Yun, S. H., Zebker, H., Segall, P., Hooper, A., & Poland, M. (2007). Interferogram formation in the presence of complex and large deformation. *Geophysical Research Letters*, 34(12), L12305. <https://doi.org/10.1029/2007GL029745>
- Yunjun, Z., Fattah, H., & Amelung, F. (2019). Small baseline InSAR time series analysis: Unwrapping error correction and noise reduction. *Computers & Geosciences*, 133, 104331. <https://doi.org/10.1016/j.cageo.2019.104331>
- ZAMG—Zentralanstalt für Meteorologie und Geodynamik. (1987). Austrian Seismic Network [Dataset]. International Federation of Digital Seismograph Networks. <https://doi.org/10.7914/SN/OE>
- Zhang, X., Feng, W., Du, H., Samsonov, S., & Yi, L. (2022). Supershear rupture during the 2021 Mw 7.4 Maduo, China, earthquake. *Geophysical Research Letters*, 49(6), e2022GL097984. <https://doi.org/10.1029/2022GL097984>
- Zhu, S., & Yuan, J. (2020). Physical mechanism for severe seismic hazard in the 2010 Yushu, China, earthquake (Mw = 6.9): Insights from FEM simulations. *Geomatics, Natural Hazards, and Risk*, 11(1), 2123–2146. <https://doi.org/10.1080/19475705.2020.1832150>